Experimental Aspects of...

Higgs Boson Searches at the LHC

Chris Tully

PiTP, IAS Princeton, Summer 2005

References:
- F. Gianotti and M. Mangano, "LHC physics: the first one-two year(s)...", hep-ph/0504221.
- M. Kado and C. Tully, "The Searches for Higgs Bosons at LEP", ARNPS (2002) 52:65-113.

An interesting comparison can be made between the experimental approach to the Higgs boson searches at LEP with those under preparation for the LHC. After early experimental measurements closed the door to the possibility of a Standard Model Higgs boson with a mass in the range $0-60$ GeV, a new era of direct searches for on-shell diboson(ZH) production began in 1996 when LEP increased the center-of-mass energy above ~ 160 GeV and continued through 2000 to the ultimate LEP energy reach of $\sqrt{s} = 209$ GeV. During this time, the event signatures were categorized according to the decay modes of the predicted Higgs boson and the well-studied decay widths of the Z boson, as shown in Figure 1.
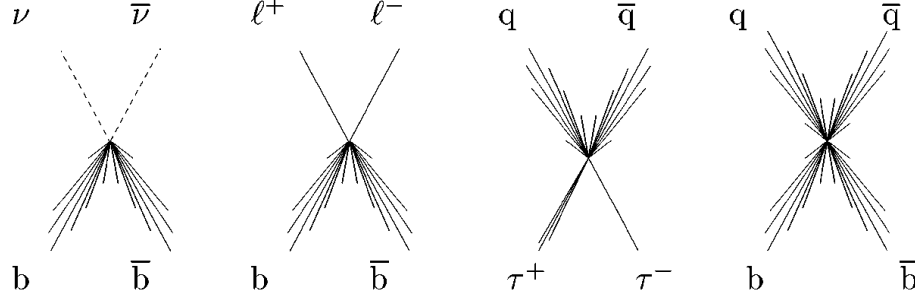

Figure 1: Topologies involved in the search for the standard-model Higgs boson at LEP2, missing energy, lepton pairs, $\tau^+\tau^-$, four-jets.

Coverage was essentially complete ($\sim 90\%$) achieving a maximum detection efficiency with varying degrees of sensitivity to the observation of a Higgs boson above Standard Model background processes with similar experimental signatures. The closest "Higgs-like" backgrounds came from ZZ production with at least one Z boson decaying to $b\bar{b}$, noting the finite and non-Gaussian detector resolution on the measurement of the dijet $b\bar{b}$-mass. An example four-jet event is shown in Figure 2.

Many analysis techniques were used to quantify the agreement of the overall contributions of Standard Model processes to the Higgs search background predictions, and in all cases the level of agreement was exceptional with comparably small theoretical and experimental uncertainties. Therefore, background systematic uncertainties have little contribution to the overall search sensitivity. An important aspect of the LEP searches was the use of full-event discrimination that was sensitive to event counting as well as properties such as reconstructed mass. The final LEP measure of the Higgs search data quantified both mass and rate information, as shown in Figure 4, where the presence of a Higgs boson signal formed a minimum in the likelihood ratio.
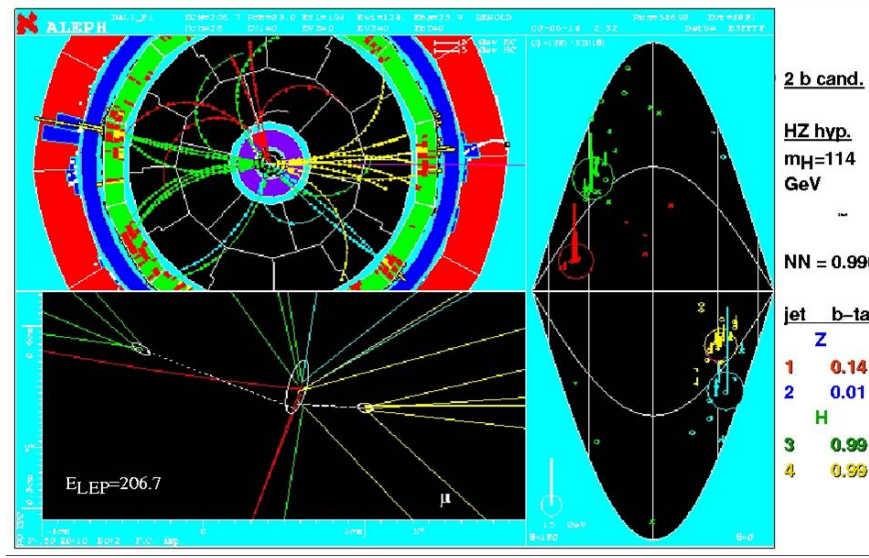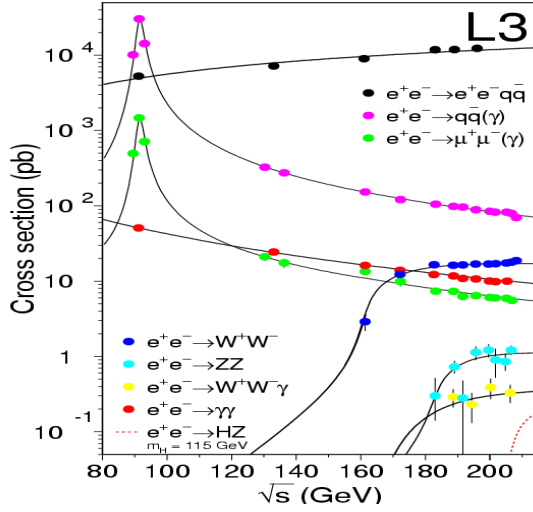
Figure 2: ALEPH four-jet event.

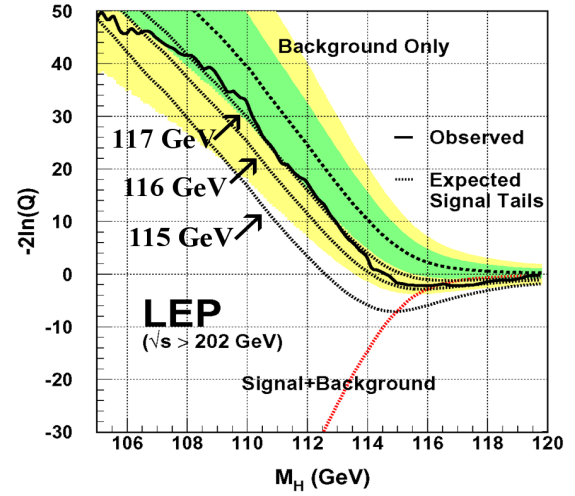Figure 3: Cross section measurements by the L3 Experiment at LEP2.

Figure 4: LEP-combined SM Higgs Search Data.

LEP was thoroughly limited by statistics at the highest achievable energies as the ZH cross section turns on rapidly above threshold, as shown in Figure 3. With four LEP experiments, sensitivity to a 60 fb cross section at the kinematic limit of $m_H = \sqrt{s} - m_Z$ was achieved with ~ 200 pb^{-1} delivered per experiment. In the missing energy channel of the Higgs search, some contribution to the sensitivity came from WW fusion, a process whereby both the incoming positron and electron covert to neutrinos radiating W bosons which fuse to form the Higgs boson, as shown in Figure 5. This exceptional process becomes a larger fraction of the total Higgs

production rate with increasing beam energy. An example missing energy event is shown in Figure 6.
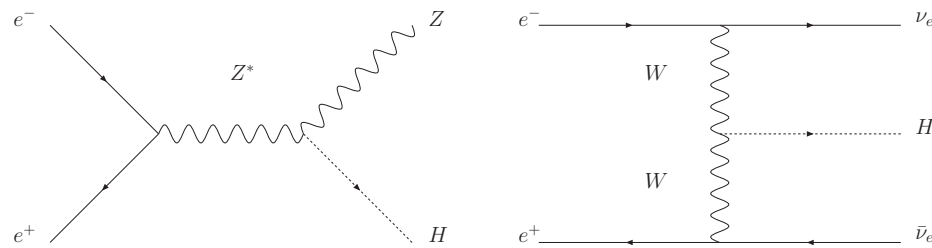

Figure 5: Diagrams of the Higgs-strahlung and weak boson fusion processes of Higgs boson production at LEP2.
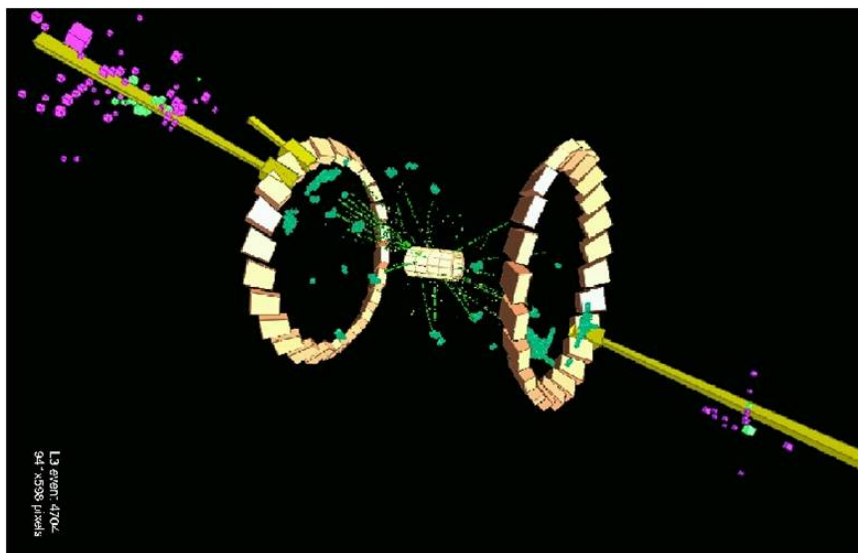

Figure 6: L3 missing energy event.

At the LHC, the approach of creating a full matrix of predicted Higgs production and associated decay processes is still a necessary starting point for the construction of the analyses, while judicious choices of processes are needed to accommodate the triggering capabilities of the experiment. There is less reliance on singular search channels in particular for channels involving jets and transverse missing energy. Search channels with multijet QCD backgrounds tend to be more inclusive in order to simultaneously fit the dominant Standard Model background fractions. Some backgrounds are necessarily estimated using data-based samples as opposed to Monte Carlo simulation. The possibility of concurrent signals such as from multiple Higgs bosons and the presence of SUSY particle production also warrant wider event sample scrutiny, not to mention the large experimental challenges of commissioning the detector in all necessary aspects of the measurement.

The justification for the many experimental "warning flags" for LHC analyses is discussed in the following

sections. The many possible manifestations of the Higgs boson discovery and crucial first measurements are also discussed.

1.1 Probing Deep within the Proton

The first step towards understanding phenomenology at the Large Hadron Collider is to quantify the influence of the proton parton distribution functions(PDF).

PDFs describe the fraction of the proton momentum x carried by the quarks, anti-quarks (by flavor) and gluons at a scale Q^2 in momentum transfer corresponding to the hard collision.

1.1.1 Parton Model for Proton-Proton Collisions

The initial kinematics are described by the incoming proton momentum, $P = 7$ TeV, and partons i with longitudinal momentum fractions, x_i ($0 \leq x_i \leq 1$). The 4-momenta and center-of-mass energy are approximated by:

$$p_{1,2} = x_{1,2}P \qquad \hat{s} = x_1 x_2 s = \tau s \tag{1}$$

and the *rapidity y* is given by

$$y = \frac{1}{2} \ln \left(\frac{E + p_z}{E - p_z} \right) = \frac{1}{2} \ln \frac{x_1}{x_2} \tag{2}$$

with $x_{1,2} = \sqrt{\tau} e^{\pm y}$.

Exercise: Show rapidity differences Δy are invariant under longitudinal boosts.

Answer:

$$E \rightarrow E' = \gamma E + \gamma \beta p_z \text{ and } p_z' = \gamma \beta E + \gamma p_z$$

Therefore,

$$y' = \frac{1}{2} \ln \left(\frac{\gamma E + \gamma \beta p_z + \gamma \beta E + \gamma p_z}{\gamma E + \gamma \beta p_z - \gamma \beta E - \gamma p_z} \right) = y + \frac{1}{2} \ln \left(\frac{1 + \beta}{1 - \beta} \right)$$

Therefore, $\Delta R = \sqrt{\Delta \phi^2 + \Delta y^2}$ is an invariant angular measure. Note, in the limit of massless particles

$$E \pm p_z = p(1 \pm p_z/p) = p(1 \pm \cos \theta)$$

$$y \rightarrow \eta = \frac{1}{2} \ln \left(\frac{1 + \cos \theta}{1 - \cos \theta} \right) = -\ln \tan \frac{\theta}{2}$$

where η is the pseudo-rapidity.

For computing transverse components of momenta, note the relationship $\sin \theta = 1/\cosh \eta$.

PDF distributions are fits to experimental data and theoretical extrapolations. An online source for these databases is:
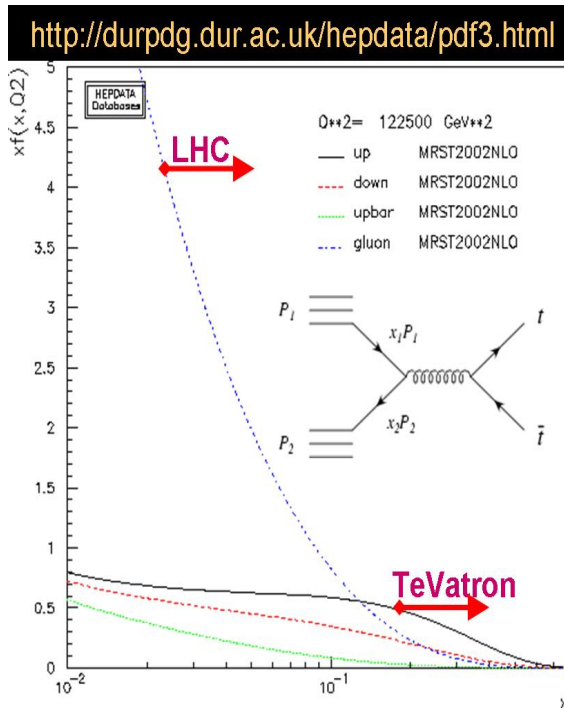
http://durpdg.dur.ac.uk/hepdata/pdf3.html

Figure 7: The PDF distributions for $Q^2 = 4m_t^2$, showing that the Tevatron had to be a $p\bar{p}$ collider for the top quark to be discovered in 1995.
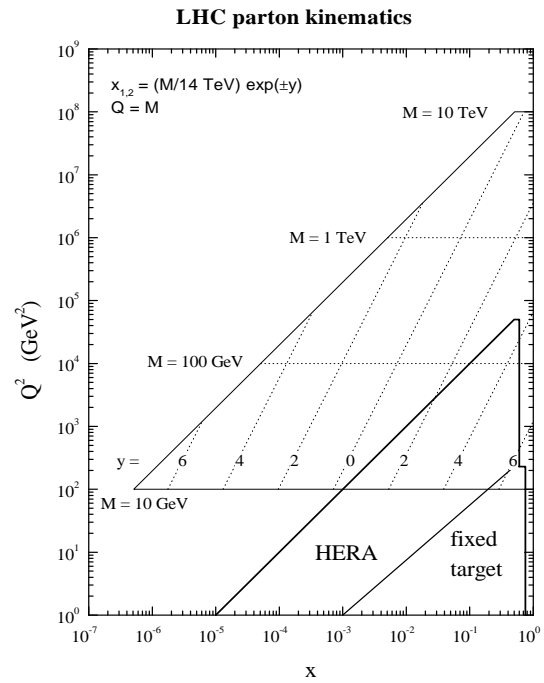

Figure 8: Regions of Q^2 and x to be probed at the LHC.

The relationships (1) and (2) can be tested against the rapidity distributions of W and Z boson production at the Tevatron. Using max. $x = 1$, the Z boson can be produced for rapidities satisfying

$$1 \geq \frac{m_Z}{1.96 \text{ TeV}} e^y \tag{3}$$

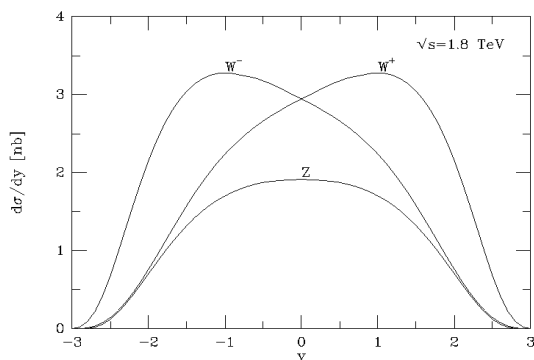which gives $y < 3$, as shown in Figure 10.

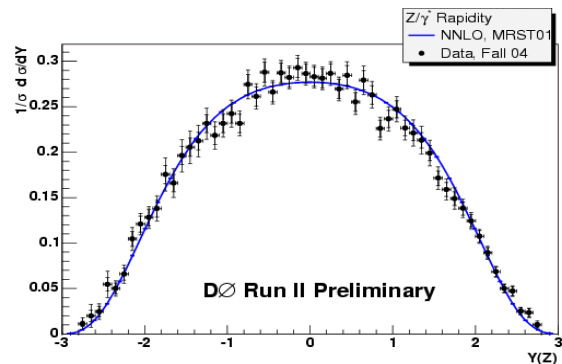Figure 9: Charge asymmetry of W bosons at the Tevatron.

Figure 10: Rapidity of Z bosons produced at the Tevatron.

The W boson rapidity has a charge asymmetry due to the larger x-values of the u-(anti)quarks in the (anti)proton compared to d-(anti)quarks, as shown in Figure 9. At the LHC, the Z bosons will be peaked backward and forward, corresponding to which proton supplied the (low x) antiquark for the $q\bar{q}$ annihilation.

1.2   More Orders of Magnitude than EWK to GUT
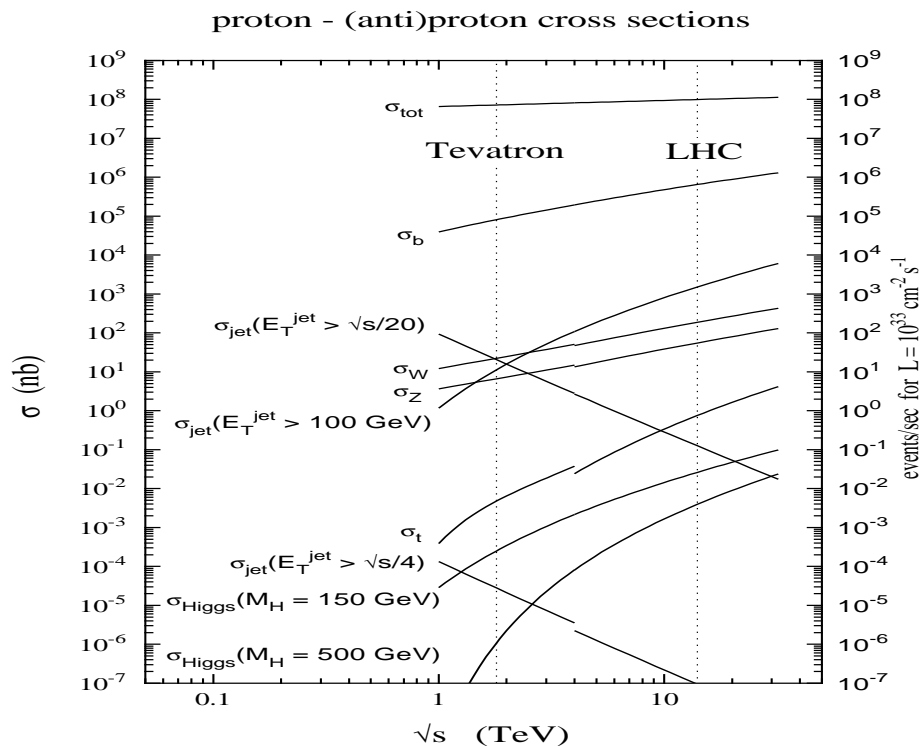
The LHC will begin taking data in 2007 with an initial target luminosity of $\mathcal{L} = 2 \times 10^{33} cm^{-2} s^{-1}$. Approximately 400 W, 100 Z bosons and 2 $t\bar{t}$ pairs will be produced per second.

Experiments handle the large spectrum of rates with trigger systems. For instance, low p_T dijet production is the dominant process at hadron colliders. While at the same time, high p_T dijets probe the smallest length scales. Measuring the cross section over a range of 10 orders of magnitude is important as it yields a running value of $\alpha_s(Q^2)$.
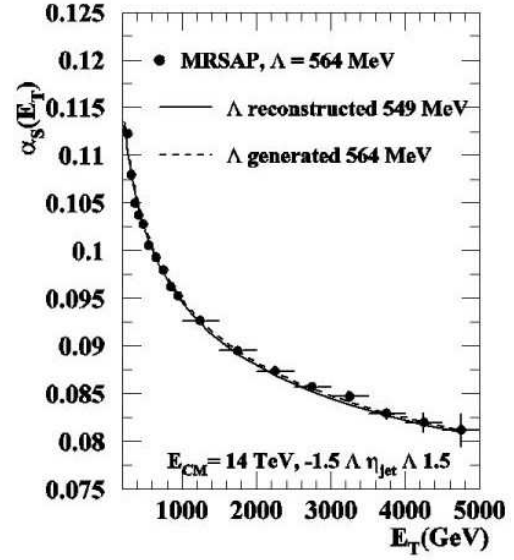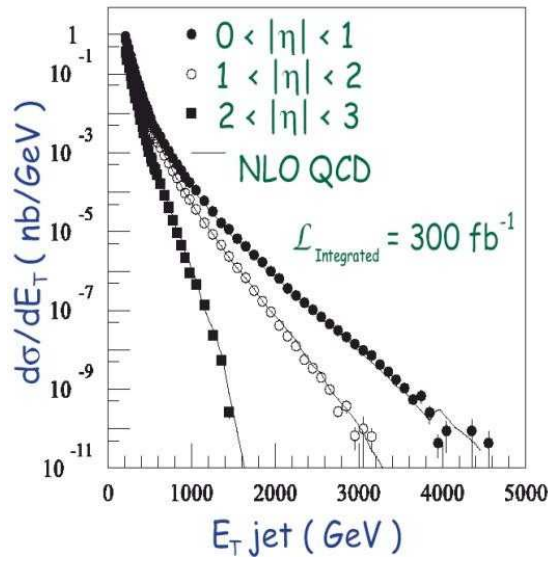
This type of spectrum is recorded with separate triggers, each of which having a different jet p_T threshold and prescales (only every N events recorded).

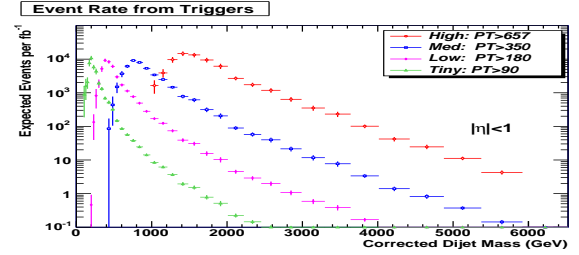| Jet Trigger Path	L1 Jet Trigger			HLT Jet Trigger			Jet Total Prescale
	$P_T(E_T)$ (GeV)	Prescale (1 / N)	Rate (KHz)	$P_T(E_T)$ (GeV)	Prescale (1 / N)	Rate (Hz)	
High	177	1	~ 1	657	1	0.31	1
Med	177	1	~ 1	350	30	0.33	30
Low	177	1	~ 1	180	600	0.45	600
Tiny	90	20	~1	90	600	0.48	12,000

Figure 11: Dijet trigger prescales.

Figure 12: Dijet events from triggers.

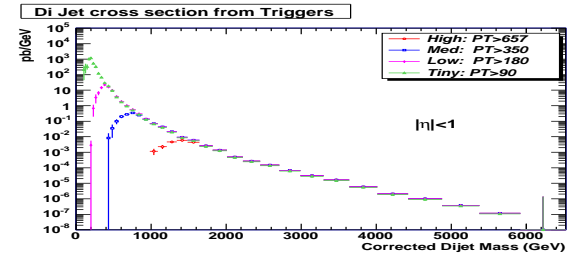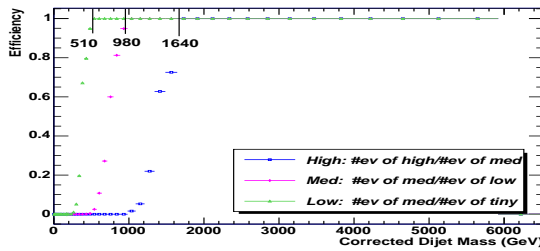Figure 13: Trigger turn-on curves.

Figure 14: Dijet cross section.

The actual cross section measurement is a piece-wise assembly of several separate triggers. Only fully efficient regions of the trigger are kept and the lowest trigger is dropped from the analysis. The turn-on curve for a trigger is a function of the jet resolution and detector uniformity. In these examples, the dijet mass spectrum is covered

down to 500 GeV with prescales, and only 2 TeV dijet resonances are in unprescaled trigger regions.

All datasets are heavily affected by the trigger or triggers used to select them. The trigger path defines a narrow sieve through which a tremendous downpour of multijet QCD events could pass, most of which as instrumental backgrounds to be defined loosely as anomalous measurements due to finite detector resolution or coverage. Tables 15 and 16 show initial estimates for the hardware and software online trigger thresholds, respectively, for the CMS experiment.

Table 15-1 Level-1 Trigger table at low luminosity. Thresholds correspond to values with 95% efficiency.

Trigger	Threshold (GeV or GeV/c)	Rate (kHz)	Cumulative Rate (kHz)
Inclusive isolated electron/photon	29	3.3	3.3
Di-electrons/di-photons	17	1.3	4.3
Inclusive isolated muon	14	2.7	7.0
Di-muons	3	0.9	7.9
Single tau-jet trigger	86	2.2	10.1
Two tau-jets	59	1.0	10.9
1-jet, 3-jets, 4-jets	177, 86, 70	3.0	12.5
Jet * E_T^{miss}	88 * 46	2.3	14.3
Electron * Jet	21 * 45	0.8	15.1
Minimum-bias (calibration)		0.9	16.0
TOTAL			16.0

Table 15-24 High-Level Trigger requirements at low luminosity. The thresholds correspond to the values in E_T or P_T with 95% efficiency (90% efficiency for muons). There is no actual threshold in the HLT selection for τ-jets, so the threshold shown is that of the corresponding Level-1 Trigger requirement.

Trigger	Threshold (GeV or GeV/c)	Rate (Hz)	Cumulative Rate (Hz)
Inclusive electron	29	33	33
Di-electrons	17	1	34
Inclusive photons	80	4	38
Di-photons	40, 25	5	43
Inclusive muon	19	25	68
Di-muons	7	4	72
Inclusive τ-jets	86	3	75
Di-τ-jets	59	1	76
1-jet * E_T^{miss}	180 * 123	5	81
1-jet OR 3-jets OR 4-jets	657, 247, 113	9	89
Electron * Jet	19 * 45	2	90
Inclusive *b*-jets	237	5	95
Calibration and other events (10%)		10	105
TOTAL			105

Figure 15: Level-1 Trigger Table.   Figure 16: High-Level Trigger Table.

The total acceptance rate to tape for an LHC experiment is ~ 150 Hz (event sizes are ~ 1 MByte). The rate of leptonic W decays alone exceeds the bandwidth. The rate of Z boson dileptons is ~ 10 Hz. If we had purely electroweak processes, then the triggers could manage this task easily. However, the rate of dijet $b\bar{b}$ production where at least one B-hadron semileptonically decays is over 10^5 Hz exceeding the hardware trigger limitations. Dijet $b\bar{b}$ production is a lepton factory. Therefore, the only way to control the single and dilepton triggers is to require the leptons to be isolated from jets, as most "soft-lepton"-tagged b-jets will contain the lepton within $\Delta R < 0.5$ separation. Jet directions are difficult to reconstruct at hardware-level, so most online isolation criteria are based on "hollow cones" centered on the lepton candidate, either in the calorimeter at level-1 or including the tracks at the higher-level software trigger. Lepton isolation criteria will have to fight against inefficiencies from underlying event, pile-up and magnetic field spreading of low p_T pions.

The trigger rates at the LHC startup will be a major test of the preparatory work in progress at the CMS and

ATLAS experiments. If the initial trigger rates exceed expectation, methods to tighten isolation criteria to control the rate will be invaluable. Directly raising the thresholds on jets and leptons will cut into vital Higgs boson signal efficiencies.

1.3   Multijet QCD Backgrounds

With such a high rate of multijet events, a single electron trigger, for example, will select some number of jets as electrons. This can be due to fragmentation or detector response fluctuations or other, that are difficult to model with finite Monte Carlo simulation statistics. Data-driven estimates are required for singly-important selection criteria, for example, a high p_{T} isolated electron.
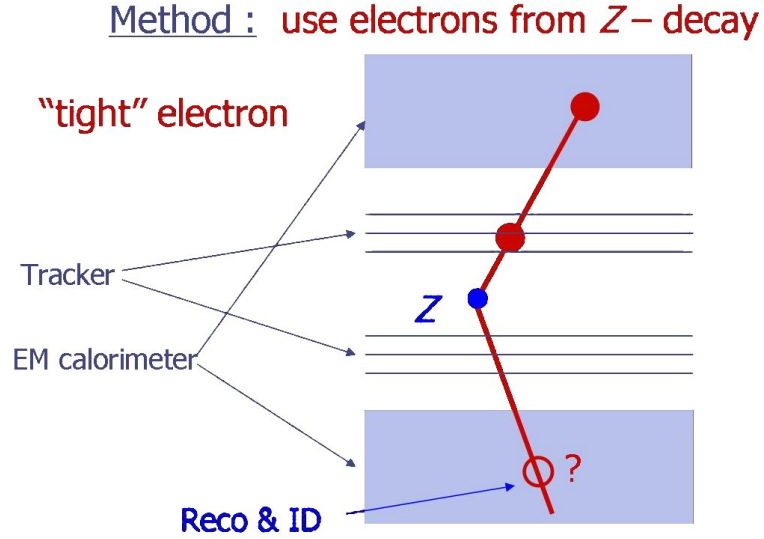

Figure 17: To verify the MC prediction for the signal efficiency ϵ_{sig}, the data-to-MC efficiencies are compared using a "tag and probe" method on $Z \to$ ee data.

One technique to determine the normalization of the multijet background is to apply a "matrix method" from simultaneous equations sensitive to the differences in behavior when tightening electron identification. One defines two samples, tight and loose. The efficiency for a true isolated electron to pass the tight cuts is given by ϵ_{sig} and for multijet background to pass a fake electron, the efficiency is ϵ_{QCD}. The set of linear equations are therefore:

$$N_{loose} = N^{sig} + N^{QCD}$$

$$N_{tight} = \epsilon_{sig}N^{sig} + \epsilon_{QCD}N^{QCD}$$

(4)

The efficiency ϵ_{sig} may be taken from Monte Carlo simulation after data-to-MC scale factors are applied, see "tag and probe" in Figure 17. Note, the normalization depends on the jet multiplicity in the event.

The efficiency for fake electrons to pass the tight cuts is measured directly from data. For example, for signals

with transverse missing energy, the low $\not{E}_T$ region will be dominated by background, and ϵ_{QCD} is the ratio of tight to loose events in this background-enhanced sample, as shown in Figure 18.
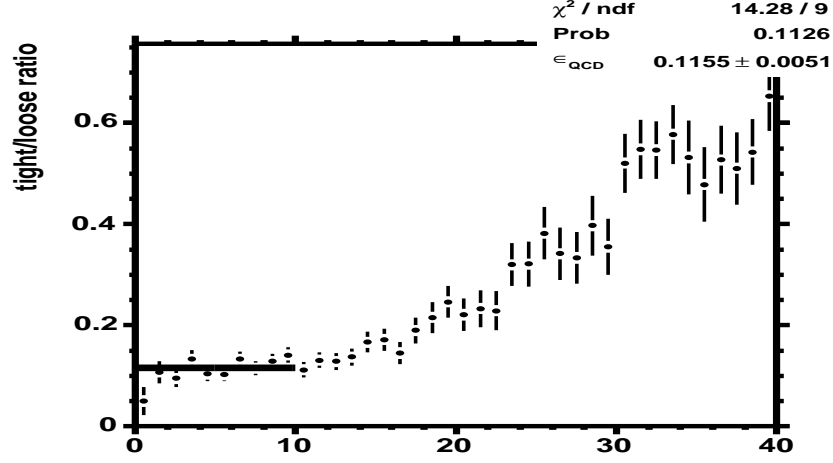

Figure 18: Ratio of tight to loose as a function of $\not{E}_T$ where extrapolation to the low $\not{E}_T$ region gives a stable value for ϵ_{QCD}.

The value of ϵ_{QCD} can depend strongly on shape and threshold parameters in the trigger selection. The background shape is taken directly from the background-enhanced sample and added to the prediction with the matrix method normalization, as shown in Figure 19.
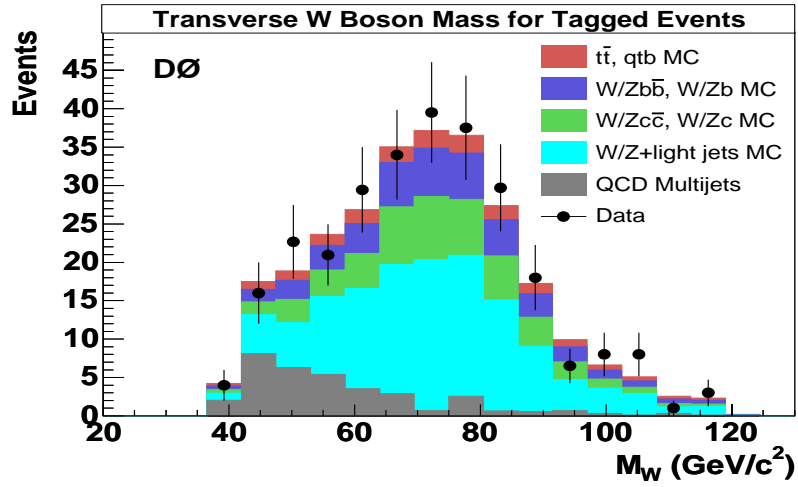

Figure 19: Example of the leptonic W transverse mass from the Tevatron in events with at least one b-tagged jet. Background shape from QCD multijets is in grey with a normalization determined from the "matrix method".

Folding the Higgs production cross sections and branching fractions (Figs. 20 and 21) against the trigger and selection efficiencies, a preliminary list of relevant search channels for a low mass Higgs search can be formed. This is given in Table 1. Of the channels in the left-most column, only the diboson decays of the Higgs are

DECAY	Production	Inclusive (including gg fusion)	Weak boson fusion	WH/ZH	ttH
$H \rightarrow \gamma\gamma$		YES	YES	YES	YES
$H \rightarrow bb$					YES
$H \rightarrow \tau\tau$			YES		
$H \rightarrow WW^{*}$		YES	YES	YES	
$H \rightarrow ZZ^{*}, Z \rightarrow \ell^{+}\ell^{-}, \ell=e,\mu$		YES			
$H \rightarrow Z\gamma, Z \rightarrow \ell^{+}\ell^{-}, \ell=e,\mu$		very low			

Table 1: The most important SM Higgs channels for m_H below the WW-threshold.

sufficiently clean to be detected inclusively within corresponding specific trigger paths. The columns to the right are a set of exclusive decay channels where identification of associated production particles give at least an order of magnitude improvement in signal to background separation, relative to the inclusive searches. The exclusive channels have unique sensitivities to 3rd generation Higgs couplings, tree-level electroweak couplings and more precise mass and partial decay width measurements.

In the 20 GeV mass range between the WW and ZZ-thresholds, the inclusive WW channel is the dominant decay mode with substantial statistics to form a transverse mass measurement of the Higgs. Above the ZZ-threshold, the four-lepton decay is the golden channel for Higgs discovery with low backgrounds and high resolution mass reconstruction in a mixture of pairs of dielectron and dimuon decays.

At the highest masses, the dropping production cross sections are compensated by the addition of hadronic W and Z decay modes. The high p_T boson signature has lower backgrounds and the dijets begin to merge, providing a clear massive monojet signature. Similarly, the neutrino decays of high p_T Z bosons provide a substantial transverse missing energy. These highly boosted diboson decays provide Higgs boson search coverage up through 1 TeV where the width of the Higgs becomes comparable to its mass and the electroweak scattering of massive weak bosons will begin to form resonances in a semi-strong coupling regime.
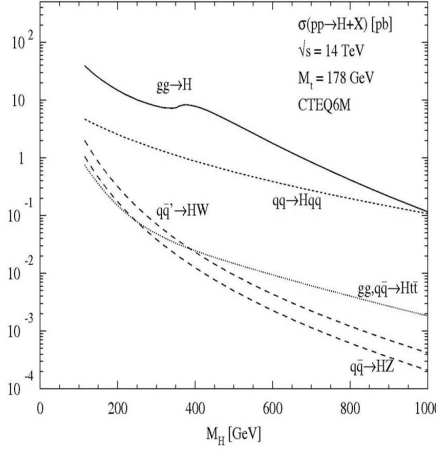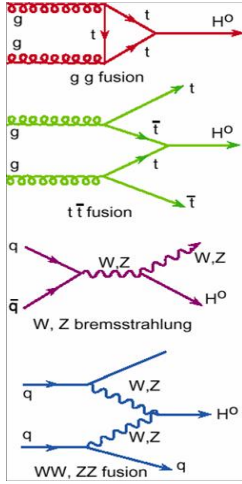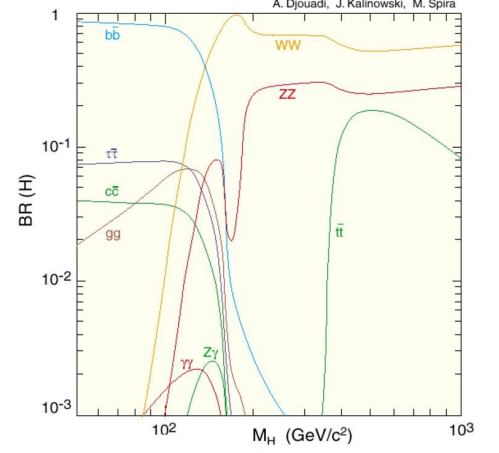
Figure 20: SM Higgs Production Cross Sections.

Figure 21: SM Higgs Decay Branching Fractions.

2.1 High Mass Resolution Search Channels

The sub-threshold decay of the Higgs boson to ZZ^* is kinematically similar to the semileptonic b-quark decay in that dominantly one Z boson is nearly on-shell and the second Z boson has a mass corresponding to the remaining Q^2 of the decay. Therefore, a 130 GeV Higgs boson will decay into a ~ 90 GeV and a less than 40 GeV pair of Z bosons. The soft Z boson decay into leptons is problematic in terms of lepton backgrounds and reconstruction efficiency. Ultimately, low p_T lepton detection and diminishing ZZ^* branching fraction limit this channel to above 130 GeV.
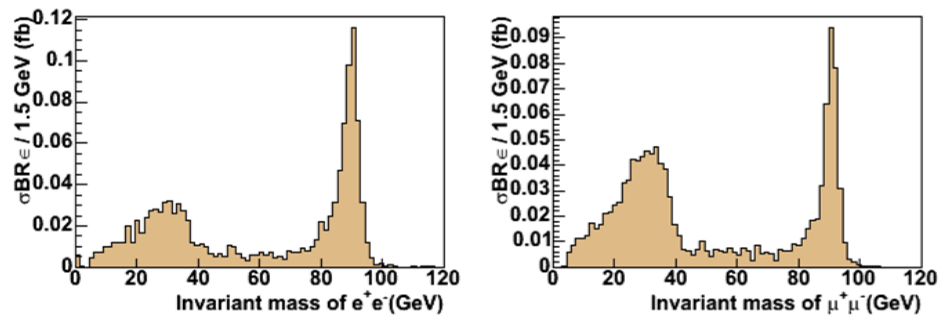

Figure 22: Dilepton mass distributions for $H \rightarrow ZZ^* \rightarrow 2e2\mu$, $m_H = 130$ GeV, on the left for dielectrons and on the right for dimuons. The low mass dimuons are enhanced because of the high muon reconstruction efficiency at low p_T.

Background to $H \rightarrow 4\ell$ comes from $t\bar{t}$ dilepton decays with both b-jets producing leptons from semi-leptonic

decays. Similarly, the process $Z b\bar{b}$ is also a background with a Z decaying to leptons and each b-jet producing a lepton (for background studies replace "b" everywhere with lepton). Note, leptons from B-hadron semileptonic decay can be partially removed using impact parameter techniques (4ℓ vertex probability) as well as lepton isolation.

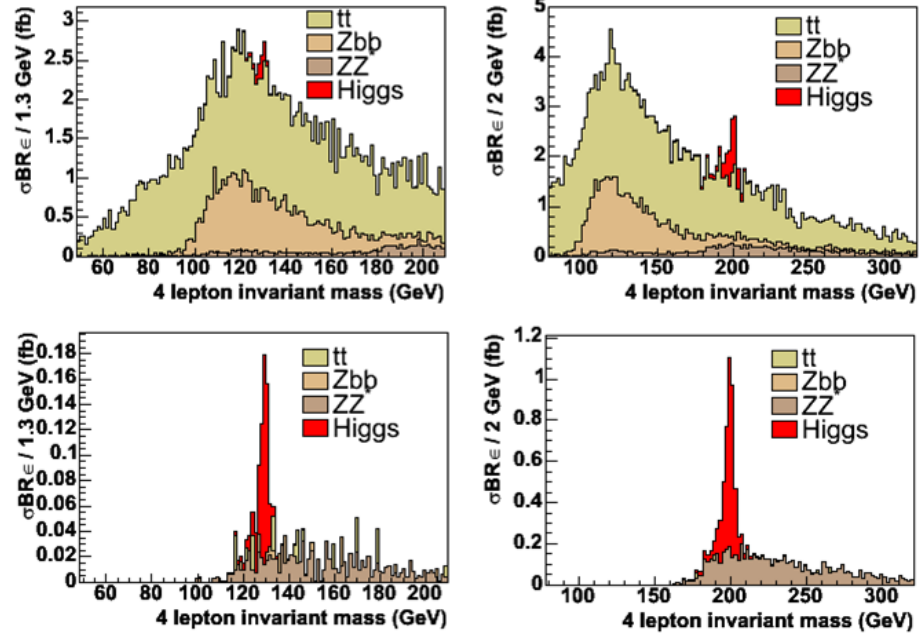The above-threshold $H \rightarrow ZZ$ decay has background from on-shell ZZ production, as shown in Figure 23. The

Figure 23: The $H \rightarrow ZZ^* \rightarrow 2e2\mu$ mass distributions before (top) and after (bottom) final selections for $m_H = 130$ GeV (left) and $m_H = 200$ GeV (right).

number of selected signal and background varies strongly with mass as shown in Figure 24 with a corresponding signal significance shown in Figure 25.   With a mass resolution of $1.0 - 1.2\%$, the direct measurement of the width Γ_H becomes possible above ~ 200 GeV as shown in Figure 26.
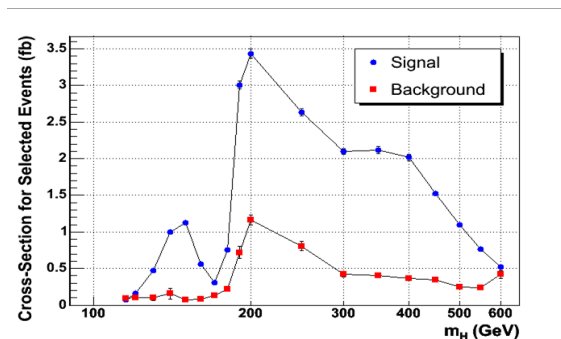
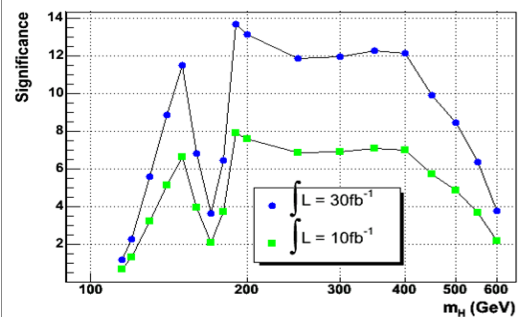Figure 24: Cross section after acceptance $H \rightarrow 2e2\mu$.

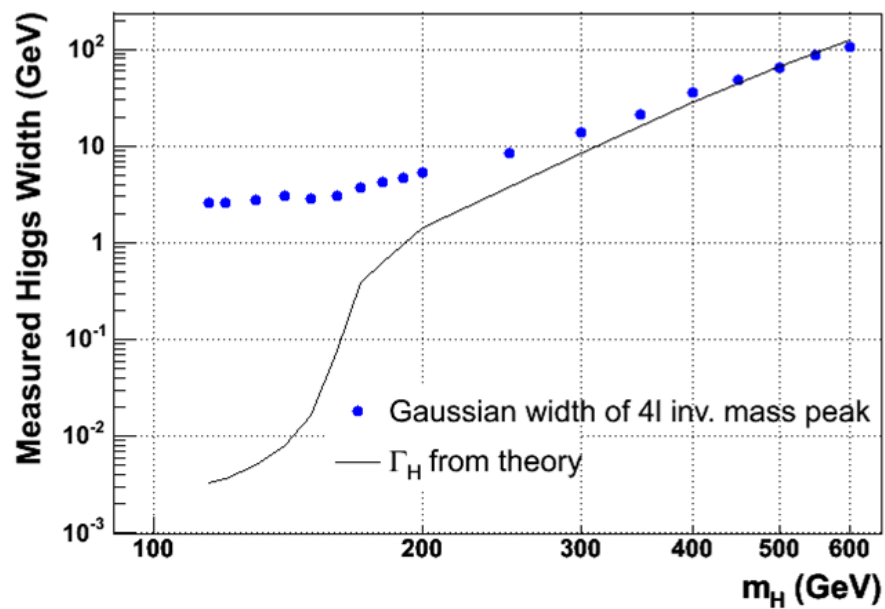Figure 25: Signal significance for $H \rightarrow 2e2\mu$.

Figure 26: Direct measurement of the Higgs width becomes possible above ~ 200 GeV in the $H \rightarrow 2e2\mu$ channel.

In addition to being a dominant discovery mode, the $H \rightarrow ZZ \rightarrow 4\ell$ decay mode is a powerful probe of the spin, parity and CP. The most general production vertex is given by

$$\frac{igM_Z}{\cos\theta_W} \left(a g_{\mu\nu} \epsilon_1^\mu \epsilon_2^\nu + \frac{b}{M_Z^2} p_{1\mu} p_{2\nu} \epsilon_1^\mu \epsilon_2^\nu + \frac{c}{M_Z^2} \epsilon_{\mu\nu\rho\sigma} p_1^\rho p_2^\sigma \right) \tag{5}$$

where the first term corresponds to the SM scalar, the second to a non-SM scalar and the third to a non-SM pseudoscalar. CP-violation would be present for admixtures of non-zero a, b and c in equation (5). The experimental observables are the azimuthal and polar angular distributions. The azimuthal angle ϕ is measured between the two planes defined by the leptonic decays of the two Z bosons in the Higgs rest frame, as shown in Figure 27. This yields a distribution

$$F(\phi) = 1 + \alpha \cos\phi + \beta \cos 2\phi \ . \tag{6}$$

The polar angle distribution has the form

$$G(\theta) = T(1 + \cos^2\theta) + L \sin^2\theta \ . \tag{7}$$

One defines the asymmetry $R = \frac{L-T}{L+T}$ to better distinguish the models. The helicity amplitude of the $|ZZ\rangle$ state
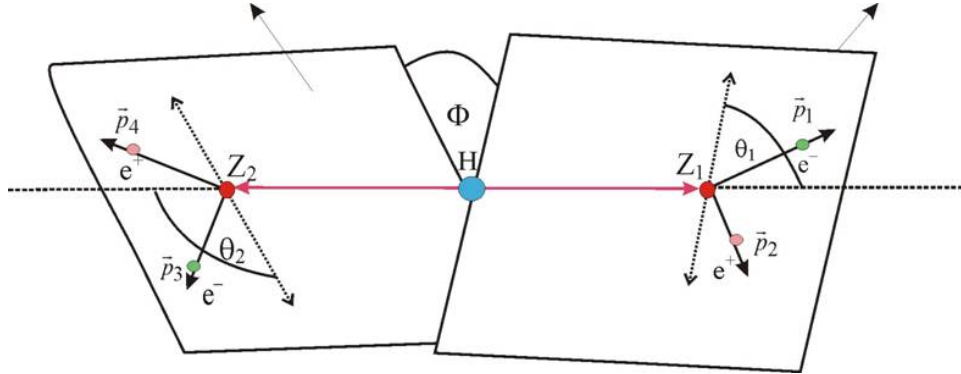

Figure 27: Definition of decay angles in Higgs reset frame.

to be in the $|00\rangle$ state is predicted to be

$$T_{00} = \frac{M_H^2 - 2M_Z^2}{2M_Z^2} \quad \text{for} \ \ M_H > 2M_Z \ . \tag{8}$$

The value of R for a $S^{CP} = 0^+$ state is $R = \frac{T_{00}^2 - 1}{T_{00}^2 + 1}$ and for a $S^{CP} = 0^-$ state, $R = -1$. The predicted values of R for SM Higgs production are given in Figure 28.
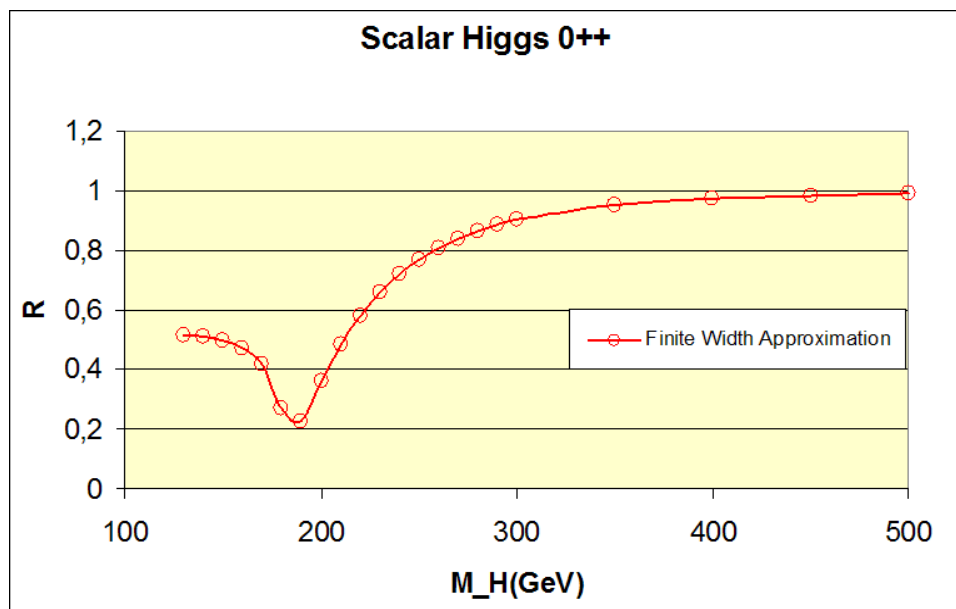
Figure 28: Standard Model prediction for R.

The $H \rightarrow \gamma\gamma$ decay is naturally expected to rise and then drop off on approaching the WW-threshold. This can

be seen from the loop-diagrams of Figure 29 which have $Q^2 \approx 4M_W^2$. The negative interference between the top
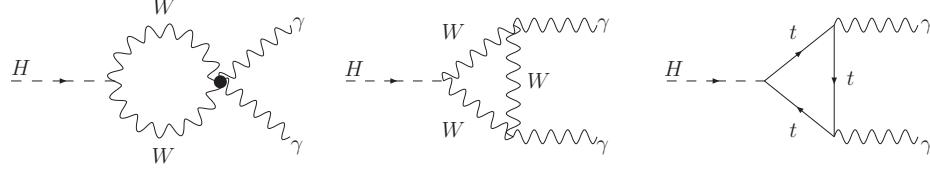

Figure 29: Loop diagrams for $H \rightarrow \gamma\gamma$ decay.

(fermion) and W boson loops decreases the partial decay width by $\sim 10\%$.

The contributions to the total Higgs production cross section at $m_H = 120$ GeV are given in Table 2. The

σ (gg fusion)(pb)	36.4
σ (IVB fusion) (pb)	4.5
σ (HW, HZ, Hqq) (pb)	3.3
Total(pb)	44.2
BR (H→γγ)	2.19×10^{-3}
Inclusive σ x BR (fb)	96.8

Table 2: Cross section and branching fraction for $H \rightarrow \gamma\gamma$.

irreducible backgrounds, i.e. those with two real photons in the final state, come from:

- $gg \rightarrow 2\gamma$ (Box diagram)

- $q\bar{q} \rightarrow 2\gamma$ (Born diagram)

- $pp \rightarrow 2\gamma + jets$ with two prompt photons

while the reducible backgrounds come from neutral jets (or hard π^0's) that fake one or two photons in the pro-

cesses $pp \rightarrow \gamma + jet$ and $pp \rightarrow jets$, respectively. The process of two neutral jets faking a pair of high energy

photons cannot be reliably simulated with Monte Carlo techniques. Data-driven techniques will be needed to

estimate these backgrounds through the process of tightening photon isolation variables using sideband regions

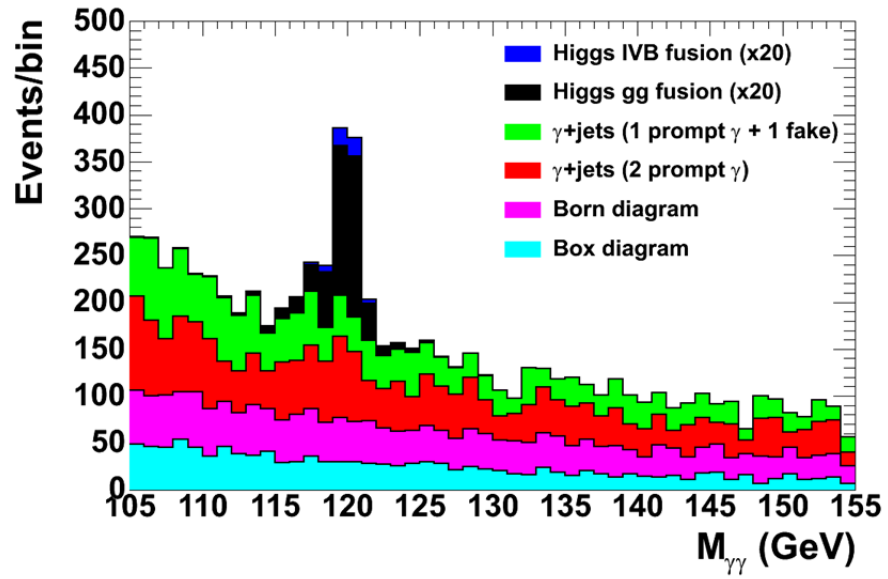of the reconstructed Higgs mass, as in Figure 30.

Figure 30: Reconstruction mass distribution for $H \to \gamma\gamma$ scale up by $\times 20$ on top of simulated background predictions. The statistics on the background predictions are low.

The overall selection efficiency for Higgs decays to photons at $m_H = 120$ GeV is $\sim 32\%$ with contributions listed in Table 3. The corresponding backgrounds for this selection are given in Table 4 with large uncertainties in the $pp \rightarrow jets$ contribution. For 1 fb^{-1} of integrated luminosity and a 2.5 GeV mass window, the expected number of $H \rightarrow \gamma\gamma$ events is 22 for a background of 535 events, giving an $S/B \sim 4\%$.

After photon selection	+tracker isol	+Ecal isol
50%	**35.3%**	**32.1±0.3%**

Table 3: Higgs selection efficiency for $H \rightarrow \gamma\gamma$, $m_H = 120$ GeV.

Box (fb/GeV)	Born (fb/GeV)	γ+ jets 2 prompt (fb/GeV)	γ+ jets 1 prompt + 1 fake (fb/GeV)	Jets (fb/GeV)	Total (fb/GeV)	$H\rightarrow\gamma\gamma$ (M_H=120 GeV) eff. in window of 2.5 GeV (%)
32	46	52	42	**41**	214	22.7

Table 4: Estimated background expectations per unit of mass window (fb/GeV) for the $H \rightarrow \gamma\gamma$ inclusive search. A typical mass window is 2.5 GeV.

The predicted $H \rightarrow \gamma\gamma$ search sensitivity depends strongly on the calorimeter resolution, as shown in Figures 31 and 32. Part of the resolution contribution is from primary vertex assignment which correctly assigns the signal vertex in $\sim 83\%$ of the events. The current technique consists of assigning the vertex with the highest p_T track in the event as the $H \rightarrow \gamma\gamma$ signal vertex.
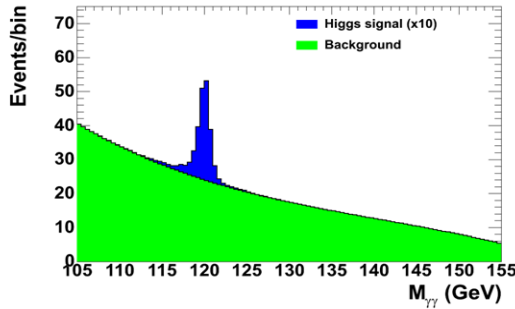

Figure 31: Comparison of signal and background distributions in $H \rightarrow 2\gamma$ for a calorimeter mass resolution of $\sigma_{m_H} = 700$ MeV at $m_H = 120$ GeV.
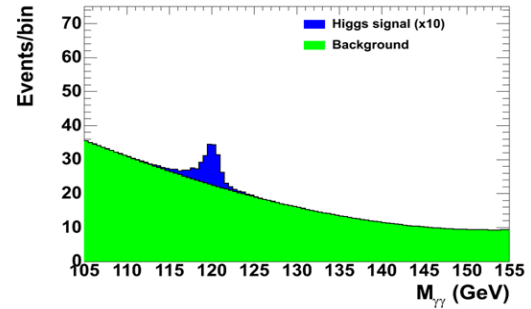
Figure 32: Comparison of signal and background distributions in $H \rightarrow 2\gamma$ for a calorimeter mass resolution of $\sigma_{m_H} = 900$ MeV at $m_H = 120$ GeV.

The gluon-gluon fusion loop-diagram for Higgs production is necessarily a high Q^2 process due to the top quark mass. It was proposed in Reference [S.Abdullin *et al.*, PLB 431: 410-419, 1998] that the search for $pp \rightarrow H \rightarrow \gamma\gamma + jet$ should have a higher signal-to-background ratio than the inclusive search, as shown in Figure 33. The backgrounds are suppressed with a cut on $\sqrt{\hat{s}} > 300$ GeV, as in Figure 34. This channel also benefits from a more efficient primary vertex-jet assignment, using the tracks of the high p_T jet to assign the signal vertex.
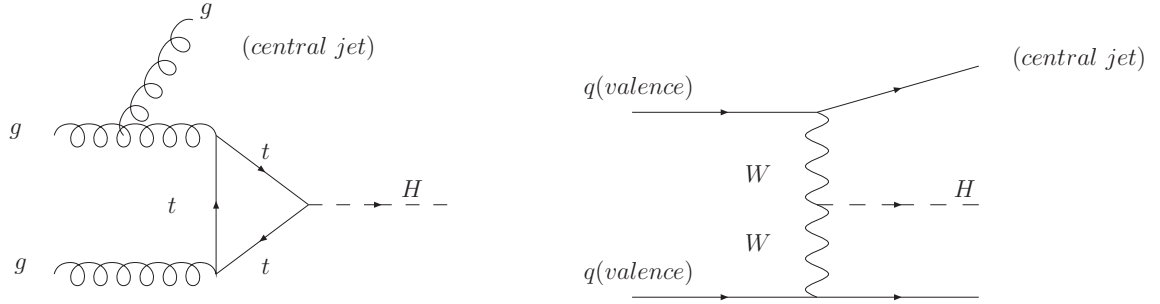
Figure 33: Two leading diagrams for $H \rightarrow 2\gamma + jet$ production. The diagram on the right is qqH weak boson fusion production of the Higgs boson.
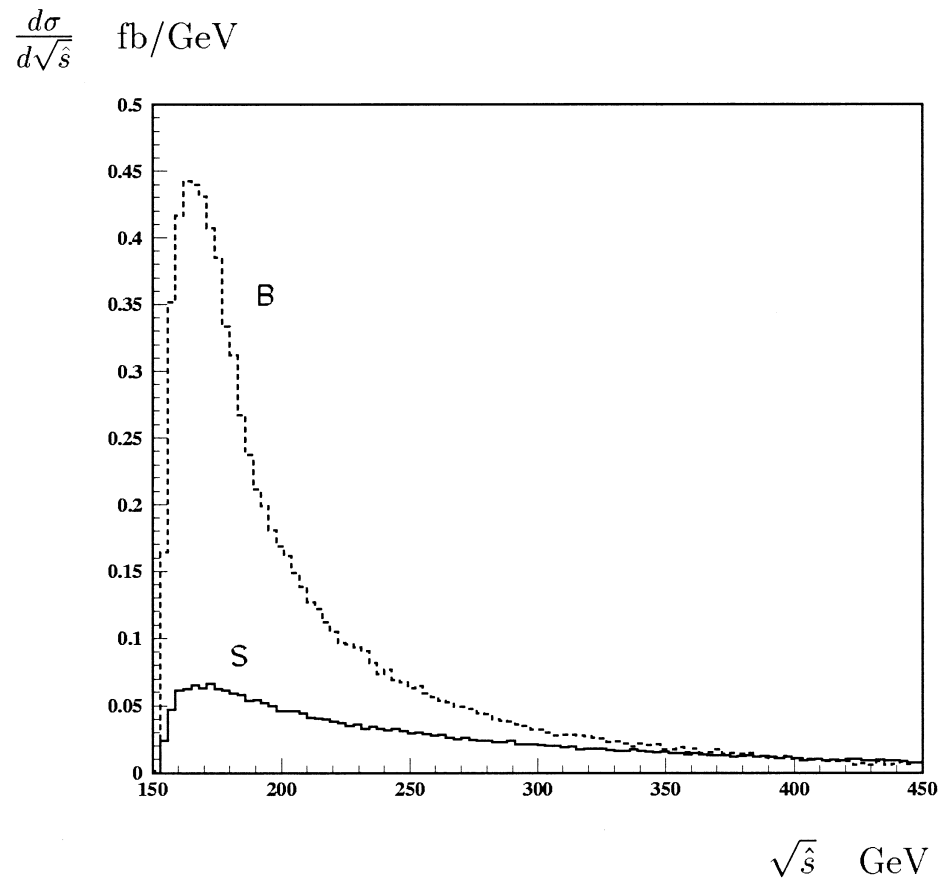
Figure 34: Distribution of the differential cross section in $\sqrt{\hat{s}}$ for the $H \to 2\gamma + jet$ signal(S) and background(B) processes.

The reduced background-level in $H \to 2\gamma + jet$ and in the weak boson fusion Higgs production will provide a flatter background shape on which to measure the mass of a light Higgs boson, as shown in Figures 35 and 36. Table 5 lists the predicted inclusive $H \to 2\gamma$ and exclusive $H \to 2\gamma + jet$ cross sections and background levels after event selection from an ATLAS analysis.
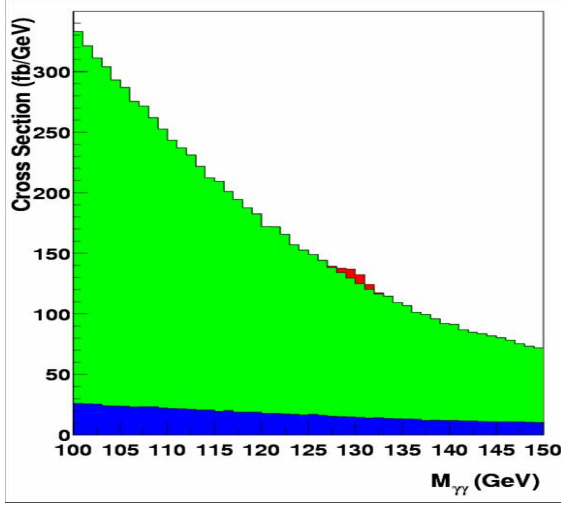
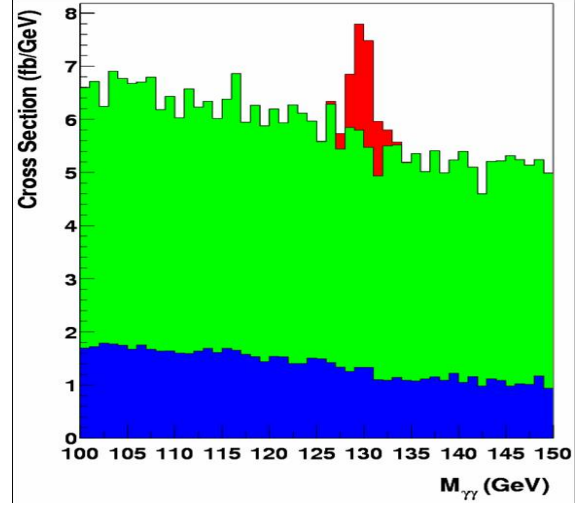Figure 35: Comparison of signal and background distributions in the inclusive $H \to 2\gamma$ search, $m_H = 130$ GeV.

Figure 36: Comparison of signal and background distributions in $H \to 2\gamma + jet$, $m_H = 130$ GeV.

Mass (GeV)		Signal: $gg \to H$ (fb)	Signal: VBF (fb)	Bkg: Real $\gamma\gamma j$ (fb)	Bkg: Fake $\gamma\gamma j$ (fb)
110	inclusive	24.16	1.68	1152.16	112.42
	exclusive	4.66	1.61	33.91	10.36
120	inclusive	23.97	1.83	803.63	90.77
	exclusive	5.25	1.89	29.89	9.17
130	inclusive	22.37	1.94	598.08	79.20
	exclusive	4.69	1.82	22.93	6.59
140	inclusive	18.35	1.94	454.17	68.89
	exclusive	3.15	1.35	13.44	4.22

Table 5: Inclusive $H \to 2\gamma$ and exclusive $H \to 2\gamma + jet$ cross sections and background levels after event selection.

2.2   JetMET-Oriented Low-Mass Channels

There are three exclusive channels in the low mass Higgs search which compete with the $H \rightarrow \gamma\gamma$ sensitivity at $m_H = 120$ GeV. These are $t\bar{t}H$ ($H \rightarrow b\bar{b}$), qqH ($H \rightarrow \tau\tau$) and qqH ($H \rightarrow WW^* \rightarrow 2\ell2\nu$), as shown in Figure 37. All of these channels involve jets and transverse missing energy in the final state, and are therefore "JetMET"-related analyses. The resolution of jet p_T measurements are roughly an order of magnitude lower (worse) than corresponding electron, muon or photon measurements, as shown in Figure 40. The lower measurement resolution reduces the reconstruction efficiency of low p_T jets and introduces fake jets formed from low energy background sources.
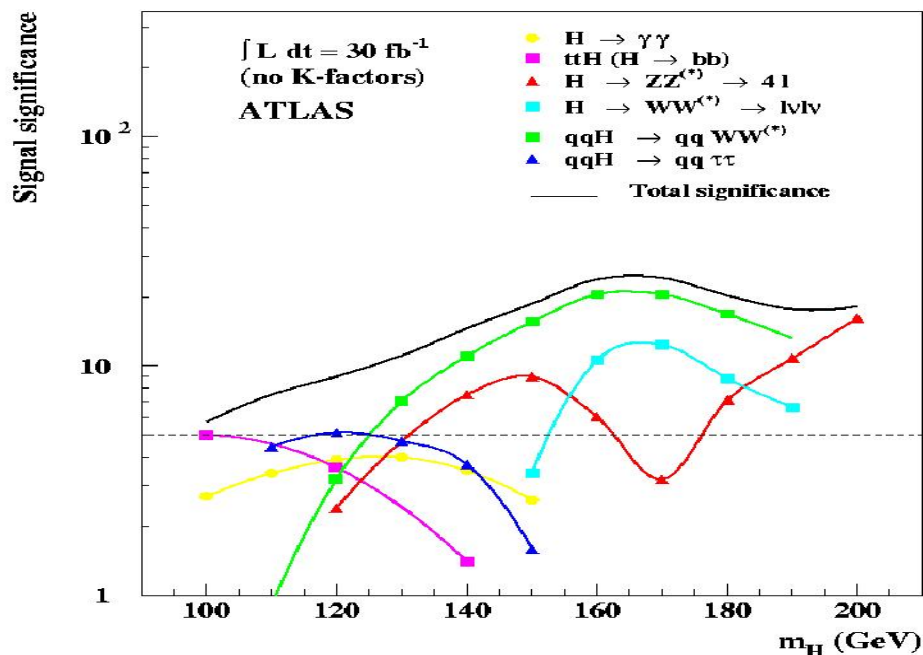

Figure 37: ATLAS Higgs search sensitivity in the low mass channels.

The cross section for $t\bar{t}$ production at the LHC is ~ 833 pb (or a factor $\times 100$ larger than at the Tevatron) and therefore an abundant source of events. Figure 38 shows a mock commissioning plot from 150 pb^{-1} of simulated initial data. The cross section for associated Higgs production $t\bar{t}H$ is ~ 0.7 pb, three orders of magnitude smaller. The $t\bar{t}H$ search channel suffers from several sources of efficiency loss from branching fractions for $t\bar{t} \to \ell + jets$ and $H \to b\bar{b}$ (total branching fraction $\sim 20\%$), single-lepton trigger inefficiency, event selection when requiring exactly six jets, jet reconstruction, combinatorics of b-jet assignment, dijet $b\bar{b}$ mass resolution and b-tagging efficiency to the fourth power, $\epsilon_b^4 \approx 11\%$. Figure 39 shows the reconstruction turn-on efficiency for jet reconstruction at an instantaneous luminosity of $\mathcal{L} = 2 \times 10^{33}~cm^{-2}s^{-1}$ in the CMS calorimeter. At parton-level, the efficiency for the $t\bar{t}H$ channel decreases from 89%, 60%, 30% to 11% for corresponding p_T cuts on all partons of 10, 20, 30 and 40 GeV. Therefore, the use of tracking and other techniques to sharpen the jet reconstruction efficiencies are essential to maintain low thresholds.
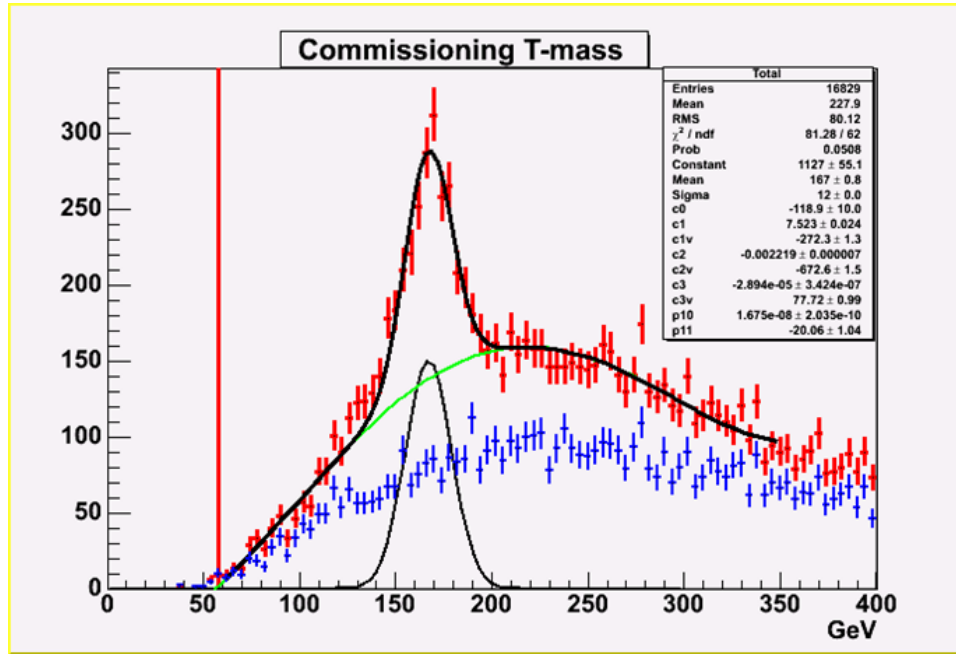

Figure 38: The three-jet hadronic top mass expected from calorimeter commissioning with 150 pb^{-1} of data.
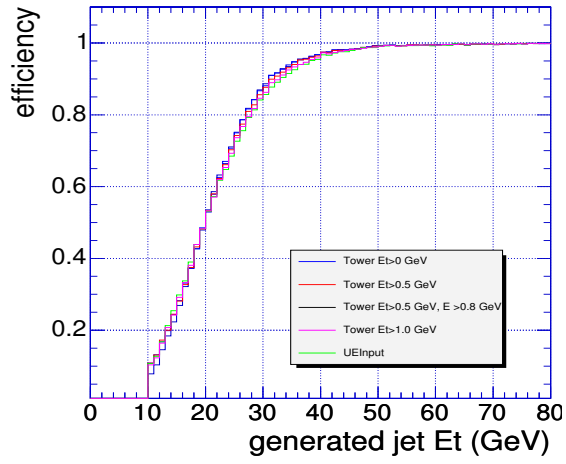
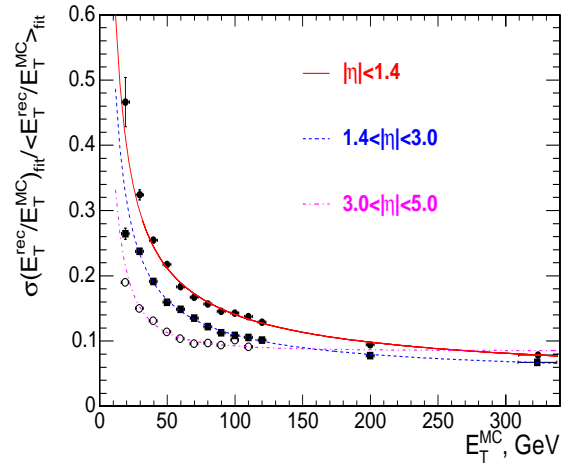Figure 39: Turn-on curve of jet reconstruction efficiency for calorimeter jets in CMS.

Figure 40: Calorimeter jet resolutions.

An example distribution of the reconstructed Higgs mass in the $H \to b\bar{b}$ decay mode in $t\bar{t}H$ events is shown in Figure 41. The background shoulder is partially due to the $t\bar{t}Z$ background with $Z \to b\bar{b}$. The $b\bar{b}$ dijet mass resolution is expect to be $\sim 12 - 15\%$ and therefore separating m_Z and m_H will be limited by detector resolutions and calibrations. There is a broad contribution to the mass distribution from $t\bar{t}b\bar{b}$ production from QCD interactions, having more theoretical uncertainties in the shape and cross section than the $t\bar{t}Z$ process.
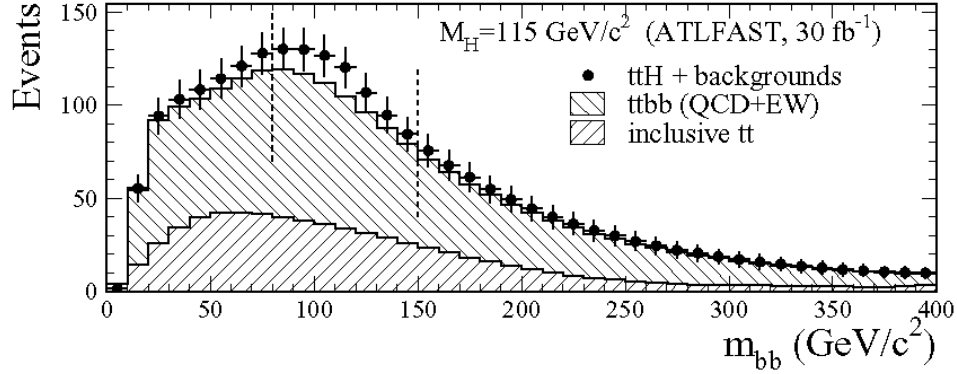
Figure 41: Higgs mass reconstruction in the $t\bar{t}H$ search.

Another JetMET-related channel is the weak boson fusion production qqH of the Higgs boson with the $H \to \tau\tau$ decay. In the decay of the Higgs to τ-leptons, a mass reconstruction technique involving the transverse missing energy aides in the separation of the large background from $Z \to \tau\tau + jets$. Only $\sim 80\%$ of the tau energy is visible in the calorimeter, the remainder is lost to neutrinos. Figure 42 shows how the transverse missing energy can be projected onto the τ-lepton momentum directions to recover part of the undetected tau energy. An example $H \to \tau\tau$ mass resolution for $m_H = 120$ GeV is shown in Figure 43.
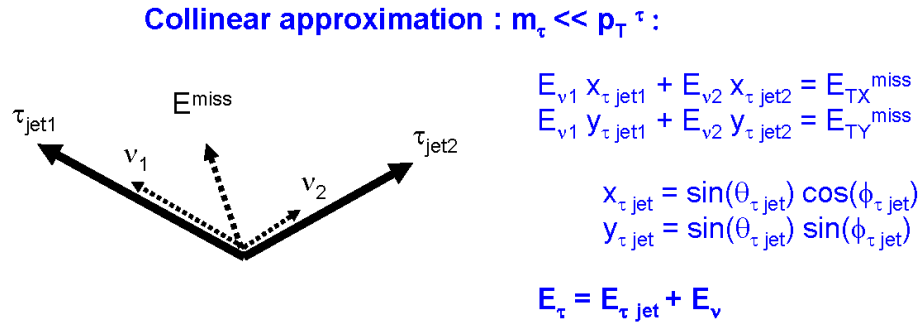
Figure 42: Mass reconstruction technique for $H \to \tau\tau$.

The effectiveness of using the measured $\not{E}_T$ depends on the $\not{E}_T$ resolution and resolution tails. Generally, the
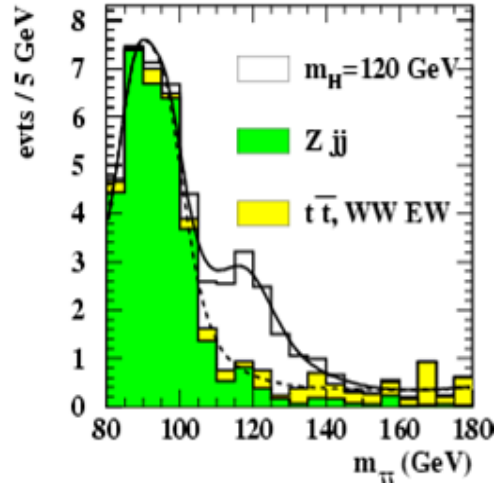
Figure 43: Reconstructed $\tau\tau$-mass using the $\not{E}_\text{T}$ projection technique in the $H \rightarrow \tau\tau$ channel.

technique in Figure 42 requires a large Higgs p_T in order to avoid false solutions. An example of $\not{E}_\text{T}$ resolution tails is given in Figure 44 for QCD dijet events, and a similar plot for the resolution as a function of the scalar $\sum E_T$ in Figure 45. The cumulative QCD $\not{E}_\text{T}$ tails set the lowest thresholds that can be used in the trigger, which is ≈ 1 Hz for a 100 GeV threshold. For events with no intrinsic $\not{E}_\text{T}$, the direction of the measured $\not{E}_\text{T}$ is correlated to the jet and lepton directions, as the mismeasurement of energetic objects is a leading source of p_T imbalance. The construction of an $\not{E}_\text{T}$ significance, or a simple requirement on the minimum angular separation of the missing energy direction and the nearest jet or lepton, can substantially reduce backgrounds from intrinsically low $\not{E}_\text{T}$ processes.
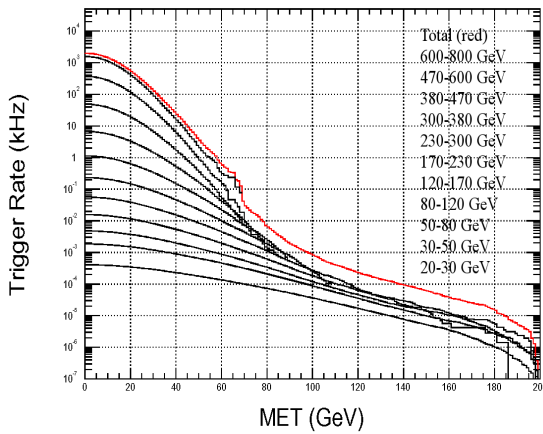

Figure 44: Transverse missing energy resolution tails in dijet events.
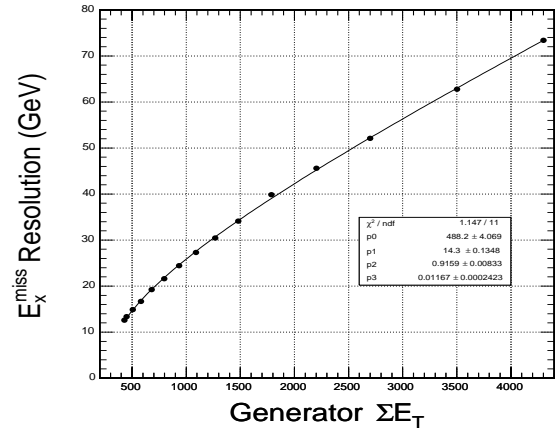
Figure 45: Transverse missing energy resolution in dijet events as a function of the scalar $\sum E_T$.

The selection efficiency for a pair of τ-leptons, such as from $H \to \tau\tau$ decay, has a substantial contribution from hadronic τ decays, as shown in Table 6. The identification of hadronic tau decays relies on the narrowness and

Final States	BR
$\tau_e \tau_h$	22%
$\tau_\mu \tau_h$	22%
$\tau_h \tau_h$	41%
$\tau_e \tau_\mu$	3%
$\tau_e \tau_e$	6%
$\tau_\mu \tau_\mu$	6%

Table 6: Tau pair final states.

isolation of the tau jet. Figures 46 and 47 show the definition and performance, respectively, of a "shrinking cone" method for separating tau jets from QCD jets. Due to the finite mass of the tau, a higher p_T boost will result in a narrower jet of particles from its decay. The dominant 1-prong and 3-prong decays of the tau and the expected visible mass distribution can be seen selected tau candidates, as shown in Figures 48 and 49 with Tevatron data.
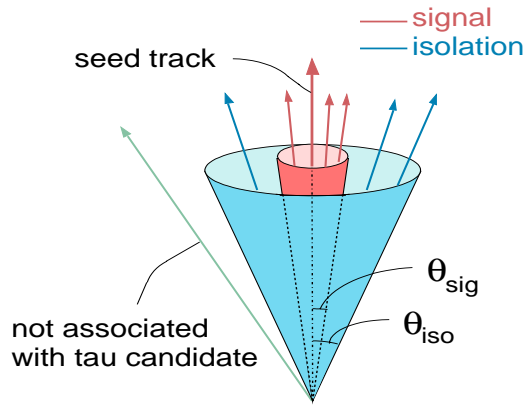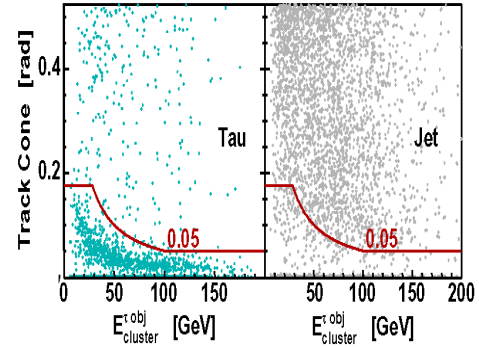

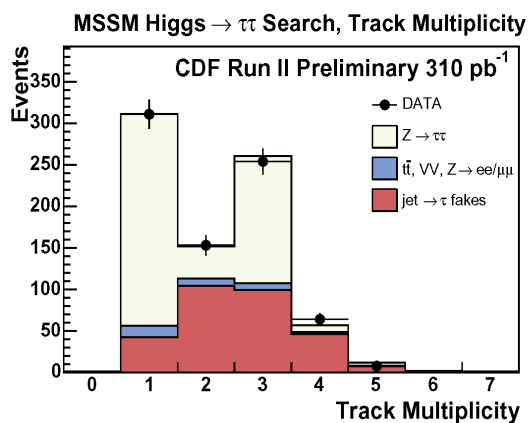Figure 46: Tau Cone Definitions.

Figure 47: Jet/Tau Separation.

Figure 48: Track multiplicity in selected τ-lepton candidates before requiring an oppositely charged pair of τ-leptons in the event.
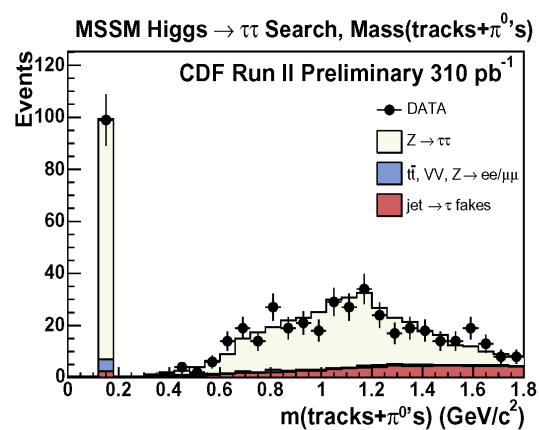
Figure 49: Reconstructed visible mass of selected τ-lepton candidates. The spike at the pion mass corresponds to 1-prong pion decays.

The triggering of qqH with $H \to \tau\tau$ relies on good hardware tau isolation techniques. Nominally, the signal signature is a four-jet final state with low $\not{E}_T$ and therefore has a potentially overwhelming multijet QCD background. However, the kinematics of the forward-jets and the narrowness of the tau jets suppresses the multijet background. The pseudo-rapidity distributions of the jets and taus are plotted in Figure 50.

An important background for the qqH search in the decay $H \to \tau\tau$ are $t\bar{t}$ events in the dilepton decay mode. The jets coming from this process are more central than forward-tagging jets from weak boson fusion and can be b-tagged if they are within the tracker acceptance, or $|\eta| < 2.4$ for CMS. Forward-tagging jets are light quark jets as they originate from valence quark scattering, see Figure 33. Therefore, the use of a central jet veto can be very powerful in reducing $t\bar{t}$ backgrounds. However, with ~ 5 multiple interactions at an instantaneous luminosity of $\mathcal{L} = 2 \times 10^{33} cm^{-2}s^{-1}$ (including single and doubly diffractive events), there are a number of minbias jets in every event with a p_T spectrum extending above 30 GeV. To maintain an effective central jet veto, the jets must be assigned to a vertex using the tracking information. The tracks of the central τ-jets define the primary vertex, and therefore the jets from the non-signal vertices are ignored in the central jet veto. Jet-vertex assignment will be important for all LHC measurements to reduce the effects of pile-up.
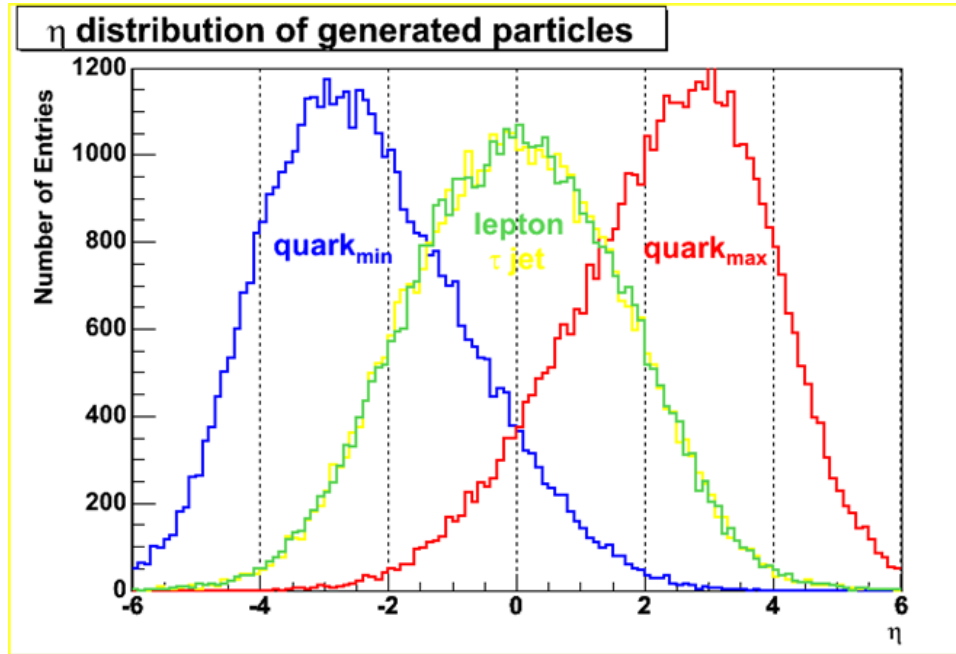

Figure 50: Forward-jet and τ-lepton pseudo-rapidity distributions in the qqH process with $H \to \tau\tau$.

2.3   Inclusive Dilepton Analysis

The $H \rightarrow WW$ decay mode has a branching fraction of $\sim 8\%$ at $m_H = 115$ GeV that grows steadily to a maximum of 96% right below the ZZ-threshold. The leptons from Higgs$\rightarrow WW$ tend to point in the same direction, as shown in Figure 51. This provides a natural search variable, namely $\Delta\phi_{\ell\ell}$ the azimuthal angle between the leptons. The high opening angle backgrounds come from $Z \rightarrow \tau\tau$ where both τ-leptons decay leptonically, as shown in Figure 52. The backgrounds in the reconstructed dilepton mass $m_{\ell\ell}$, shown in Figure 53 and 54 from the Tevatron, depend on the flavor combination of the leptons, where the $e\mu$ channel has substantially lower backgrounds from Drell-Yan and $Z \rightarrow \ell\ell$.
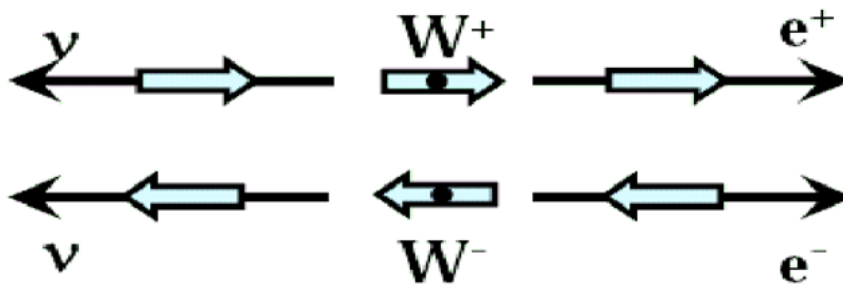

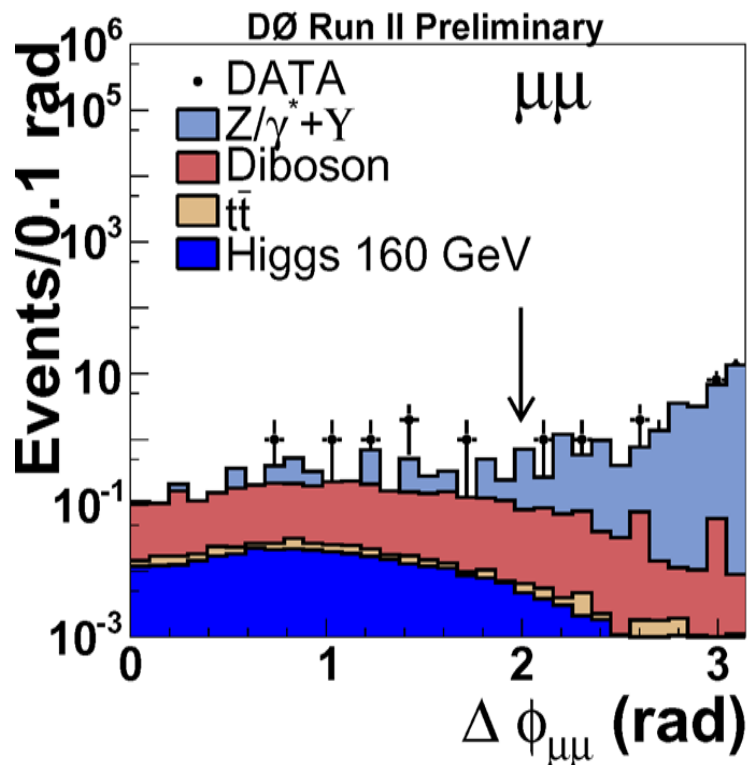Figure 51: Leptons from $H \rightarrow WW$ decay tend to point in same direction.

Figure 52: The azimuthal opening angle between leptons in the $H \to WW$ channel from the Tevatron.

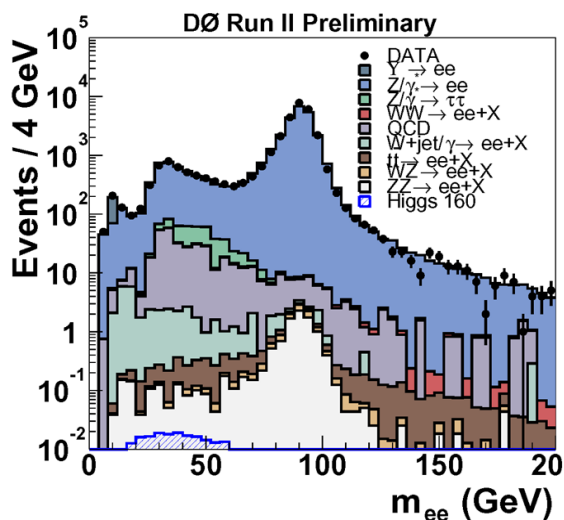Figure 53: Reconstructed dilepton mass in $H \to WW \to$ ee channel.
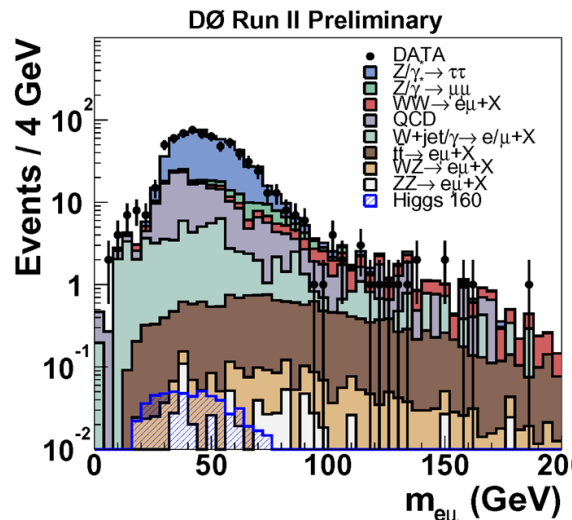
Figure 54: Reconstructed dilepton mass in $H \to WW \to$ eμ channel.

The $t\bar{t}$, WW and $Z \to \tau\tau$ backgrounds to the $H \to WW$ search have differing dilepton kinematics, jet multiplic-ities and missing energy distributions. As it will be particularly difficult to fully separate samples with differing jet multiplicities and missing energy distributions, it is likely that a simultaneous "inclusive" dilepton analysis will be applied. An example analysis from the Tevatron is shown in Figure 56. In addition, the LHC will have new backgrounds such as flavor excitation production of $gb \to tW$, as shown in Figure 55.
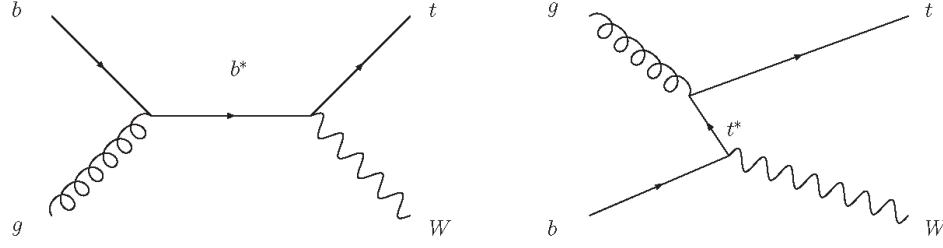

Figure 55: Flavor excitation processes contributing to the dilepton event selection.

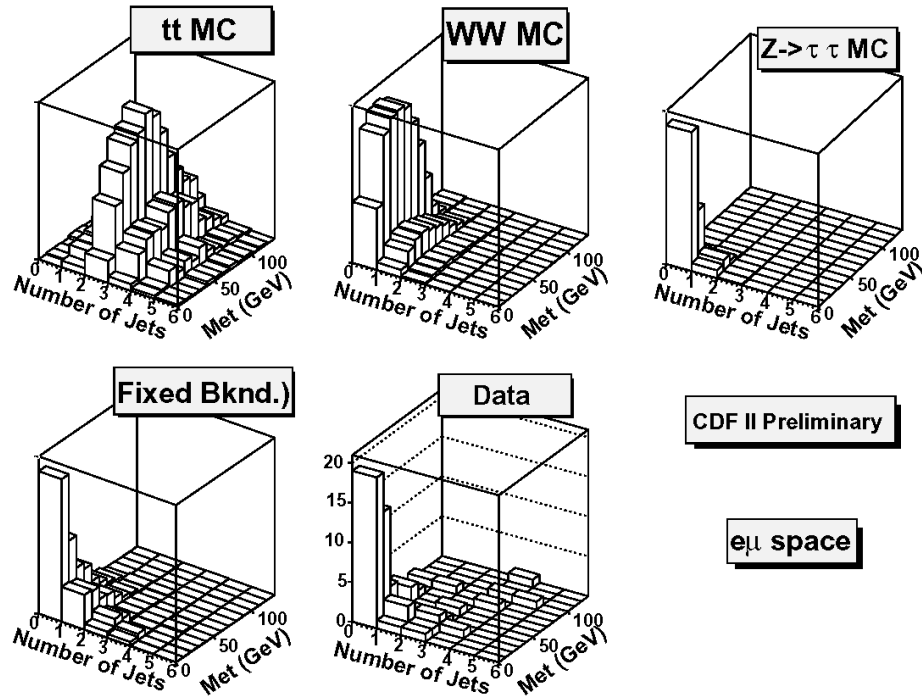

Figure 56: The 2D distributions of jet multiplicities and transverse missing energy for $t\bar{t}$, WW and $Z \to \tau\tau$ in addition to instrumental and other backgrounds.

Without direct mass reconstruction, as here only the transverse mass is available, a successful search in this channel requires an accurate normalization of standard model contributions to the dilepton event selection and well-described signal kinematics. The transverse mass distribution for $H \to WW$ at $m_H = 160$ GeV is shown in Figure 57. The effect from higher-order corrections on signal kinematics, the Higgs p_T distribution, is shown in Figure 58 and is a source of uncertainty on the dilepton distributions.
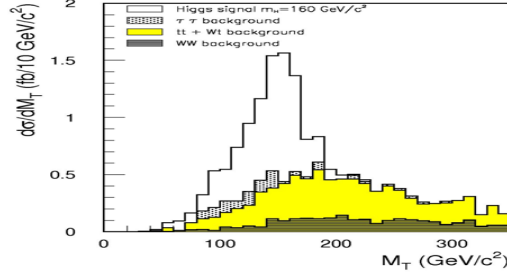

Figure 57: Transverse mass distribution in the $H \to WW \to e\mu\nu\nu$ channel with forward-tagging jet requirements.
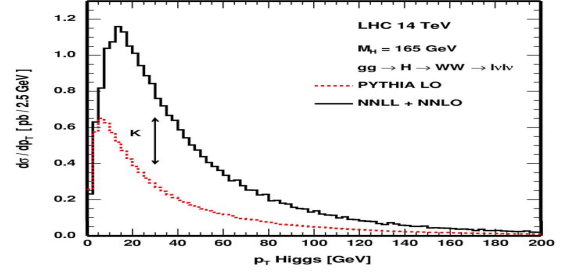
Figure 58: Leading-order event simulations are reweighted for higher-order corrections to the event kinematics.

In the sub-threshold region of the $H \to WW$ decay, the requirement of forward-jet tagging, according to the kinematics of qqH production, results in a factor of 10 reduction in background, thereby opening up the low mass search in this channel. Similarly, if the second lepton p_T is too low, then the forward-jets must be included in the trigger decision in order to reduce events from $W + jets$ and multijet QCD background as these would dominate in a single lepton trigger. Forward jets have a transverse momentum of roughly half the W mass, as expected from massive W propagators in the fusion process. The measurement of qqZ production will be an important benchmark for understanding forward jets at the LHC. The tagging jets occur in the pseudo-rapidities $1.5 < |\eta| < 4.5$ as shown in Figure 50 with corresponding energies of ~ 300 GeV or higher. Figure 59 shows an η-ϕ map of a qqH event with identified forward jets. There is a slow narrowing of jets with energy, according to the Q^2 of the jet production, that goes approximately as $E^{-1/4}$. Therefore tagging jets have a narrower energetic core than backgrounds consisting of boosted low energy jets, minbias pile-up and reminants from the underlying event.
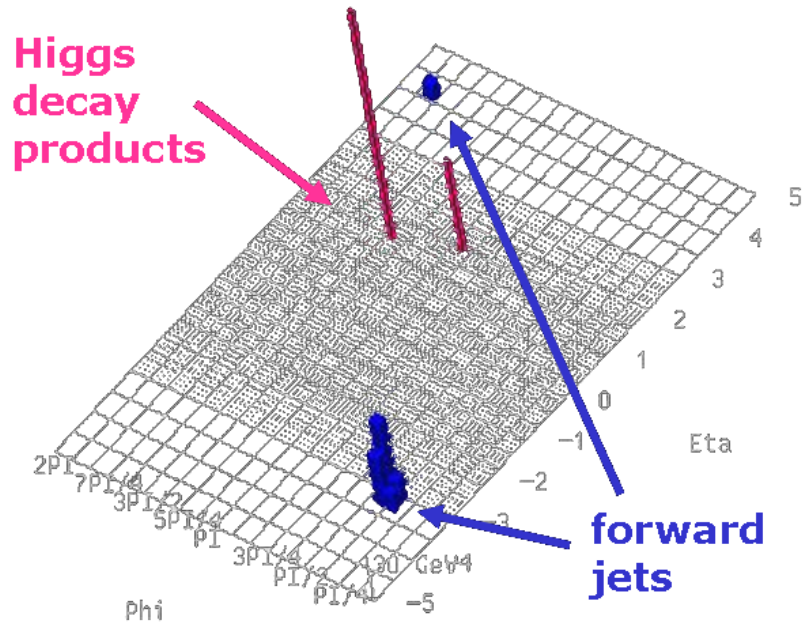

Figure 59: An η-ϕ map of a qqH event with identified forward jets.

As shown in Figure 37, the qqH channel with $H \rightarrow WW^*$ loses sensitivity when the effective W^* mass goes below $\sim M_W/2$. To continue the $H \rightarrow WW^*$ search down to lower masses, the WH production channel can be used. In this channel, there are two nearly on-shell W bosons in the $WH \rightarrow WWW^*$ process. The hard dilepton p_T spectra in this channel increase trigger efficiencies and open up the possibility of a same-sign dilepton search for half of the sample. This signature has very low physics backgrounds especially for dissimilar lepton flavors in the $e^{\pm}\mu^{\pm}$ channel. The soft third lepton may be above reconstruction thresholds, especially for muons, and therefore introduce the trilepton signature. The trilepton and same-sign dilepton searches are high purity analyses and have mainly diboson and instrumental backgrounds. The rejection of the Z peak in the WWW^* signature is effective in removing diboson backgrounds, as shown in Figure 60. The ZH production mechanism would be another source of enhanced triple boson production. The performance of the WWW^* same-sign dilepton search has been studied at the Tevatron for the low mass Higgs search and has the most stringent cross section exclusion, as plotted in Figure 61.
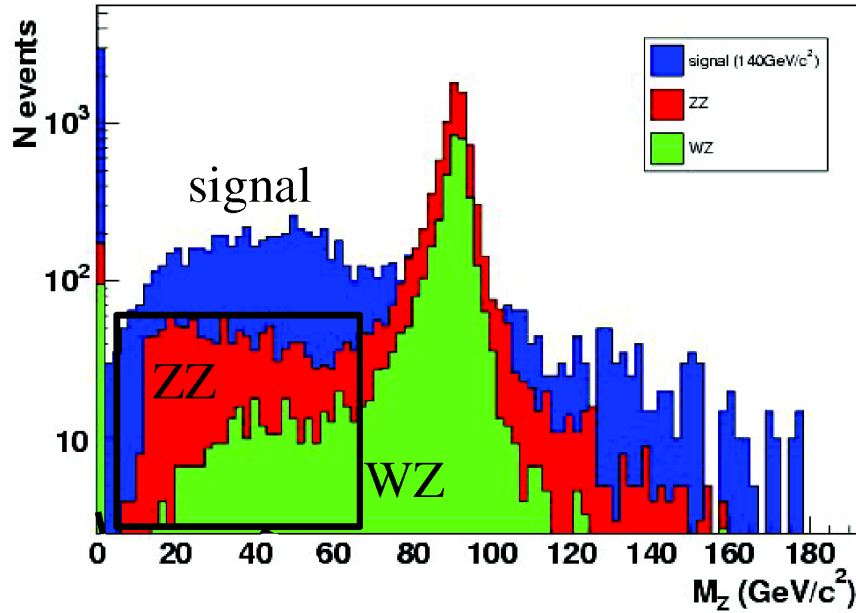

Figure 60: Presence of a Z peak in dilepton combinations from ZZ and WZ backgrounds are rejected in the trilepton $WH \rightarrow WWW^*$ channel. The ZZ backgrounds with $Z \rightarrow \tau\tau$ fall into the signal region as indicated by the boxed region.
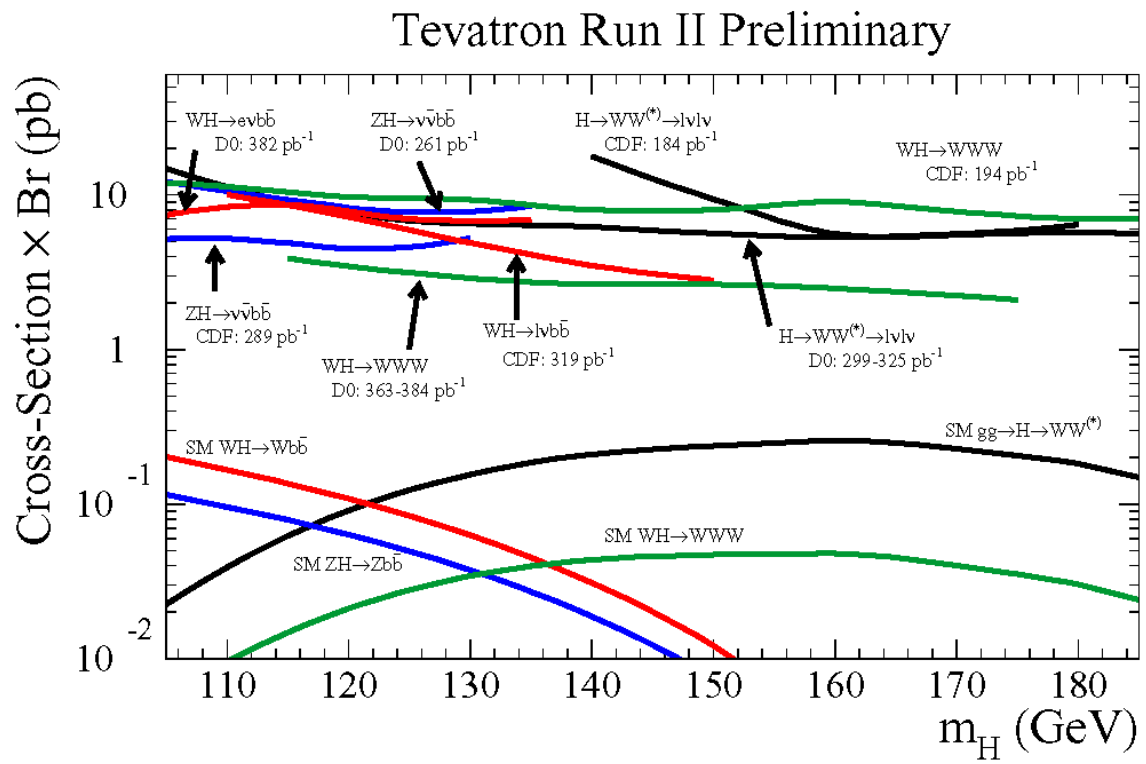
Figure 61: Overall summary of Standard Model Tevatron Higgs searches showing the WWW^* exclusion limits.

2.4   Boosted Dibosons from Heavy Higgs Decay

As shown in Figure 26, the natural width of the Higgs boson exceeds 100 GeV for a mass of $m_H = 600$ GeV and above, and the total production rate drops to below 1 pb with a significant fraction of the total rate coming from qqH production. To cover this heavy mass region, additional decay channels of $H \rightarrow WW$ and ZZ need to be utilized. The highly boosted W and Z bosons coming from an 800 GeV Higgs boson decay will have collimated decay products, as drawn in Figure 62 for the strong WW scattering process. The hadronic decays appear as single jets in the detector. The mass of the single jet can be used to identify the jet as originating from a W or Z boson, as shown in Figure 63. The qqH production mode with $H \rightarrow WW \rightarrow \ell\nu jj$ and $H \rightarrow ZZ \rightarrow \ell\ell jj$ decay modes benefit from the higher branching ratios of the hadronic boson decay, and the identification of a massive single jet is an effective part of the event signature. A similar high branching ratio decay channel is the $H \rightarrow ZZ \rightarrow \ell\ell\nu\nu$ in qqH production. This provides a large transverse missing energy signature as shown in Figure 64.
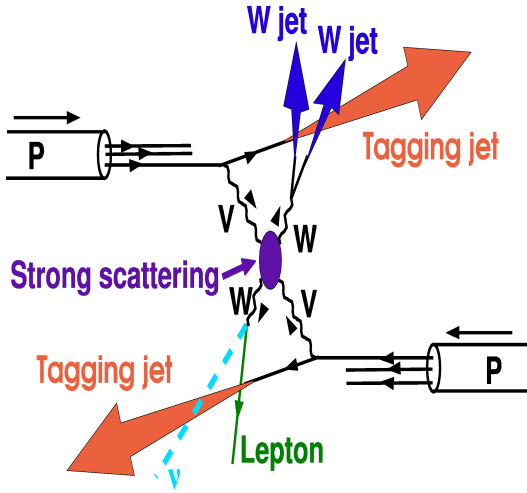

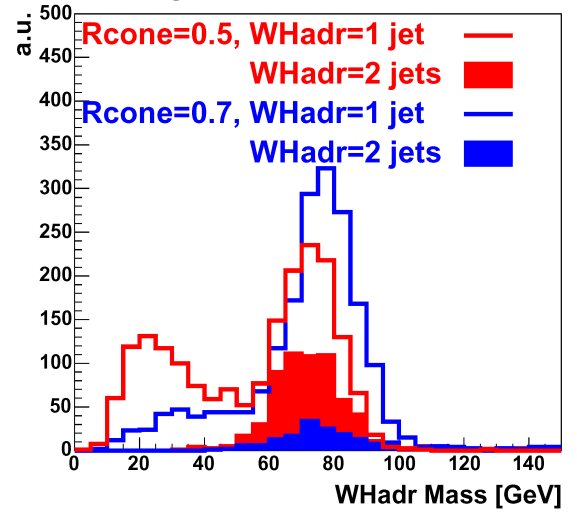Figure 62: Heavy Higgs production and strong WW scattering event signature.
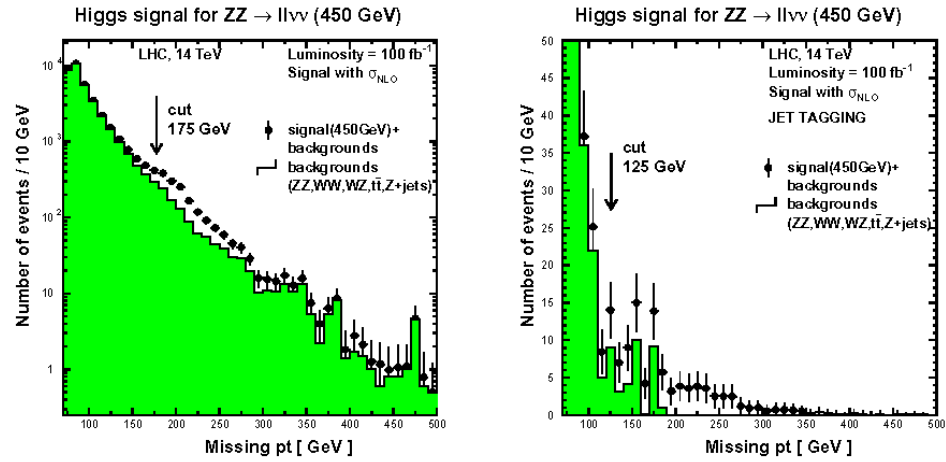
Figure 63: Single-jet W mass reconstruction.

Figure 64: Transverse missing energy distribution in $H \to ZZ \to \ell\ell\nu\nu$ channel without (left) and with (right) requiring forward-tagging jets from weak boson fusion production.

2.5   From 115 GeV to 1 TeV

An overview of the Standard Model Higgs search sensitivity with the CMS experiment is shown in Figure 65.
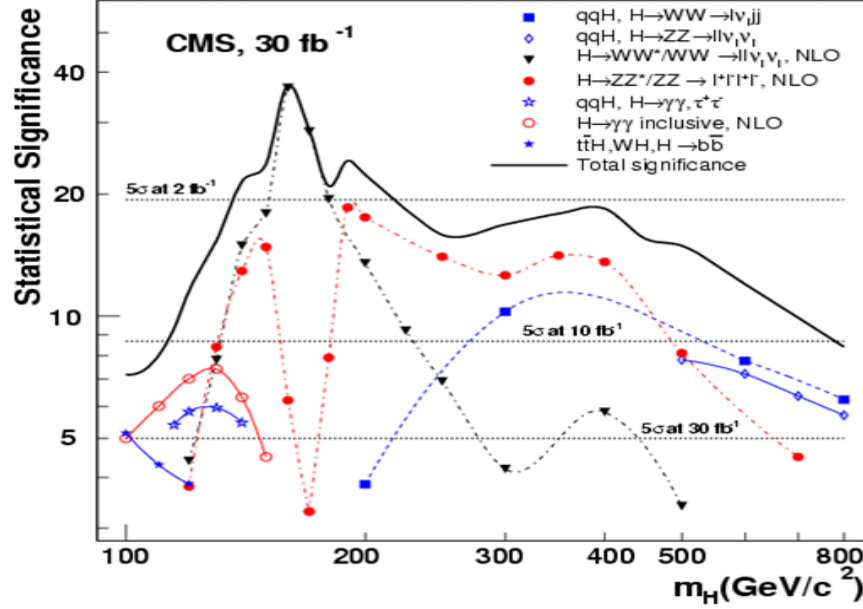

Figure 65: Estimates of the statistical significance of the Standard Model Higgs boson searches with 30 fb^{-1} of integrated luminosity.

The LHC Higgs search has a broader variety of possible analyses than those developed at LEP. Furthermore, the experimental challenges are starkly different in the different search topologies and mass ranges. The high mass resolution channels depend strongly on the calibration and alignment of the tracking, calorimeters and muon spectrometers and are subject to intense commissioning efforts. The JetMET-related search channels must contend with the low p_T jet reconstruction efficiencies and fake rates. The usage of the transverse missing energy in these channels is also subject to commissioning and the effects of detector noise, jet mismeasurement response tails and minbias pile-up. For weak boson fusion search topologies, the forward-tagging jets will be nearly the highest pseudo-rapidity jets used for analysis in hadronic collisions, creating an uncertainty in the reliability of simulations of the jet backgrounds in the forward regions. In cases where the search channel depends on efficient τ-lepton triggering or on single lepton triggers plus jets, techniques for data-driven background calculations must be applied to correctly account for multijet QCD backgrounds and instrumental backgrounds enhanced by the trigger selection. Inclusive analyses, such as the dilepton analysis, will have to address a wide variety of standard model processes, some never measured before. The same-sign dilepton and trilepton searches will address rare backgrounds processes with unknown contributions from fake and misreconstructed leptons,

requiring data-derived estimates. Heavy Higgs searches will require dedicated treatment of highly boosted W and Z boson decays.

In general, the understanding of the searches starts at high p_T and moves towards lower masses. It would not be surprising in the LHC Standard Model Higgs search to see a rapid exclusion for Higgs boson masses above $m_H \approx 150$ GeV and extending up to 500 GeV, and then followed by more detailed experimental efforts as discussed here to cover the low mass region down to $m_H = 115$ GeV and the high mass region up to 1 TeV.